



# Synthesis process and efficient NH<sub>3</sub>-SCR performance of alkali/alkaline earth metal-rich Chlorella@Mn catalyst

Hengheng Liu<sup>a,1</sup>, Fengyu Gao<sup>a,b,1</sup>, Songjin Ko<sup>a,c</sup>, Ning Luo<sup>a</sup>, Xiaolong Tang<sup>a,b,\*</sup>, Honghong Yi<sup>a,b</sup>, Yuansong Zhou<sup>a,b</sup>

<sup>a</sup> School of Energy and Environmental Engineering, University of Science and Technology Beijing, Beijing 100083, China

<sup>b</sup> Beijing Key Laboratory of Resource-oriented Treatment of Industrial Pollutants, Beijing 100083, China

<sup>c</sup> Department of Chemistry, Pyongyang University of Architecture, Pyongyang, Democratic People's Republic of Korea

## ARTICLE INFO

### Keywords:

Chlorella@Mn catalyst  
Mn<sup>2+</sup> adsorption time  
NH<sub>3</sub>-SCR  
Adsorption mechanism  
Alkali/alkaline earth metals

## ABSTRACT

Low-temperature NH<sub>3</sub>-SCR denitrification catalyst was prepared by biological method using Chlorella cells. In this process, Chlorella cells adsorbed Mn<sup>2+</sup> in manganous solution were centrifuged, dried and calcined to obtain the Chlorella@Mn catalyst, the adsorption process involved electrostatic interaction, complexation/chelation and ion exchange mechanisms. Compared with the pure MnOx catalyst, Chlorella@Mn catalyst contains 2.77% alkali/alkaline earth metals (K, Na, Ca, Mg), but still has higher NOx conversion, N<sub>2</sub> selectivity and anti-H<sub>2</sub>O poisoning, with NOx conversion close to 100% at 100–225 °C. Chlorella@Mn catalyst surface possesses more acidic species, K, Na, Mg on the surface mainly exist in the form of K<sub>2</sub>SO<sub>4</sub>, NaPO<sub>3</sub> and MgSiO<sub>3</sub>, respectively, Ca mainly exists as amorphous Ca<sub>x</sub>Mn<sub>y</sub>O<sub>z</sub>, and the presence of Ca can inhibit the over-oxidation of NO. Biological methods have more advantages such as simple process and low cost, this study will provide some reference for the preparation of novel denitrification catalysts by biological methods.

## 1. Introduction

With the development of economic globalization, industrial wastewater discharges are increasing, among which wastewater containing heavy metals has a serious impact on the ecological environment and human health, and the treatment of heavy metal pollution has become an urgent problem [1,2]. Heavy metals in wastewater mainly include cadmium (Cd), lead (Pb), copper (Cu), arsenic (As), manganese (Mn), etc. Heavy metals have the characteristics of enrichment, non-degradability, persistence, etc., which make heavy metal treatment a major problem [3,4]. The current treatment methods include ion exchange, adsorption, filtration, electrodialysis, precipitation and membrane bioreactor, etc. [5,6], among them, the adsorption method has attracted more attention due to its advantages of convenient operation and wide applicability [7]. The adsorbent used is mainly carbon-based materials, but the traditional carbon-based materials have not very high adsorption performance and need to further improve its adsorption performance by physical or chemical modification, etc. [8,9]. Meanwhile, it faces the problem of adsorbent regeneration [10], which also

increases the cost and process. Although other technologies have also been applied to some extent, there are problems such as high cost, complicated process and long treatment cycle in different degrees, and some of these technologies even require secondary treatment of wastewater [10]. In view of the above problems, biosorption methods have been widely studied for their low cost, good affinity for binding heavy metals, environmental friendliness and other advantages [11,12]. In particular, some progress has been made in using active algae to adsorb heavy metals [13–15], among them, Chlorella has attracted more and more attention in the field of wastewater treatment due to its fast growth and reproduction, easy artificial cultivation, etc.

At the same time, in addition to heavy metal pollution of water bodies in the environment, the presence of NOx in the atmosphere is also one of the important reasons for environmental pollution, it can cause photochemical smog, acid rain under certain conditions [16,17]. Industrial fixed sources are one of the main sources of NOx emissions [18], industries that generate a large amount of NOx emissions include thermal power, steel, cement, etc. [19,20]. NOx emission reduction technology is mainly ammonia selective catalytic reduction technology

\* Corresponding author at: School of Energy and Environmental Engineering, University of Science and Technology Beijing, Beijing 100083, China.

E-mail address: [txiaolong@126.com](mailto:txiaolong@126.com) (X. Tang).

<sup>1</sup> These authors contribute equally to this article.

(NH<sub>3</sub>-SCR), through which NO<sub>x</sub> is reduced to pollution-free N<sub>2</sub> and discharged into the atmosphere, thereby reducing NO<sub>x</sub> pollution [21, 22]. With the development of technology and changes in application conditions, low-temperature selective catalytic reduction denitrification technology has become a research hotspot in the field of denitrification, the core of this technology is low-temperature denitrification catalyst [23]. With the deepening of research, it is found that Mn has the advantages of variable valence and good denitrification effect at low temperature [24,25], while heavy metals such as Cd, Pb, Cu and As have relatively low catalytic conversion capacity. Mn-based catalysts have become an important research and application object of low-temperature denitrification catalysts, Li et al. found that the Mn-InO-6 catalyst (Mn: In = 6:1) showed the best activity, maintaining approximately 100% NO<sub>x</sub> at conversion rates of 75–200 °C [26], Zhao et al. found that CoMn oxide calcined at 250 °C exhibited high activity, giving 91% NO<sub>x</sub> conversion at 60 °C [27]. In summary, Mn is not only one of the elements that cause heavy metal pollution in water, but also one of the important elements commonly used to prepare NH<sub>3</sub>-SCR denitrification catalyst, in view of this, we first consider using Chlorella cells to adsorb Mn<sup>2+</sup> in water to prepare denitrification catalyst. However, the presence of alkali metals (K, Na) and alkaline earth metals (Ca, Mg) in the actual flue gas will significantly reduce the denitrification performance by affecting the active sites or acidity of Mn based catalysts, and improve the anti-alkali/alkaline earth metal poisoning performance of the catalyst has become a research hotspot in the field of denitrification, Chlorella itself contains certain concentrations of K, Na, Ca, Mg. Using active Chlorella to adsorb Mn<sup>2+</sup> in water to prepare low-temperature denitrification catalyst and studying the adsorption mechanism, low-temperature denitrification activity, the existing forms and functions of alkali/alkaline earth metals, and the relevant physicochemical characteristics of the catalyst will have high research value and application prospects, which is not only conducive to the treatment of heavy metals in water, but also conducive to the removal of NO<sub>x</sub> in the atmosphere. It has dual theoretical and practical significance, but at present, there are relatively few studies in this area.

In this paper, the influence of different adsorption time on Mn<sup>2+</sup> removal in water, Chlorella cells activity and low temperature denitrification activity was studied to determine the relevant changes in the adsorption process. Through advanced characterization methods, the physicochemical characteristics of the catalyst under different adsorption time in in-situ synthesis were analyzed, and its dynamic change process was mastered to finally determine the evolution process of denitrification catalytic activity, adsorption mechanism, existing forms and functions of alkali/alkaline earth metals. Through the above research, it can not only provide some references for the active algae to adsorb heavy metals in water, but also for the development and application of bio-derived low-temperature NH<sub>3</sub>-SCR denitrification catalysts resistant to alkali/alkaline earth metal poisoning.

## 2. Experimental section

### 2.1. Synthesis of catalyst

Synthesis of the Chlorella@Mn and Chlorella denitrification catalysts: 0.6 g mass of manganese acetate tetrahydrate was added to 250 mL of fresh Chlorella solution of approximately 20 million cells per milliliter concentration to simulate manganese-containing water, stir at a slow speed for 5–8 min to dissolve manganese acetate tetrahydrate, meanwhile, the Chlorella solution contained the culture components necessary for its growth. Among them, used Chlorella cells needed to be in a good growth and reproduction stage, the reagents used were analytically pure and did not need further purification before use, the mixed solution was left to stand for different times. Then the solution was centrifuged, and the solid components were collected. After drying, it was calcined at 450 °C for 3 h, and finally ground into 40–60 mesh particles, and the samples were marked as the Chlorella@Mn catalysts. The fresh Chlorella

solution without manganese acetate tetrahydrate was labeled as Chlorella catalyst after the same treatment as above.

Under the same preparation conditions, the corresponding mass of manganese acetate tetrahydrate was added to 250 mL of ultrapure water, and stir to dissolve, after the standing time of 24 h and after drying and calcination, finally ground into 40–60 mesh particles, the prepared catalyst was labeled as the MnO<sub>x</sub> catalyst.

### 2.2. Catalyst characterization

Inductively coupled plasma (ICP) was carried out on Agilent ICPOES730 in the United States, with emission power of 1.0 KW and carrier gas of argon. The catalysts were determined by X-ray fluorescence spectroscopy (XRF) measurements using ARLAdvant'X IntellipowerTM3600 (Thermo, USA). Apoptosis was performed on flow cytometry (Luminex, model: Guava Easy Cyte), cells were stained with SYTO 9 and PI respectively, apoptosis was detected in Green-B channel and Yellow-B channel, data were analyzed with Flow Jo software. Cytotoxicity was carried out on the laser confocal microscope TCS-SP8 SR, and the pretreated cells were stained with dye solution for 5 min before taking photos. Cell morphology was observed on Hitachi TEM system HT7820. Fourier transform infrared spectrometer (FTIR) was carried out on the iS10 FT-IR spectrometer of Negoli, with a wave number range of 400–4000 cm<sup>-1</sup>, a resolution of 4 cm<sup>-1</sup>, and 32 scans. X-ray diffraction (XRD) was carried out on a Bruker: D8 ADVANCED system, Cu Kα radiation (40 kV and 40 mA) was used to determine the X-ray diffraction of the catalyst in the range of 10–90° at a rate of 5°/min. UV-vis diffuse reflection spectroscopy (UV-vis DRS) was carried out on Spectrophotometer UH4150 with the wavelength of 200–800 nm. Scanning electron microscope (SEM) was carried out on the TESCAN MIRA LMS, using Pt as the gold spraying target, the acceleration voltage was 3 kV during the morphology shooting and 15 kV during the energy spectrum shooting. X-ray photoelectron spectroscopy (XPS) was performed on an Escalab 250Xi spectrometer (Thermo, USA) equipped with Al Kα radiation (1486.6 eV), with the carbon 1 s peak (BE = 284.6 eV) used as the standard to calibrate all binding energies. Raman was carried out on Renishaw inVia, the laser wavelength was 532 nm, and the wave number range was 400–3200 cm<sup>-1</sup>. EPR was carried out on Bruker A300–10/12 in Germany, TEMPO was used as the hole trapping agent, and the reaction concentration of the trapping agent was 50 mM. TG-DSC was carried out on NETZSCH STA 449 F3/F5 and TA Q200, and the temperature range was 30–900 °C.

*In-situ* diffuse reflectance infrared fourier transform spectroscopy (*In-situ* DRIFTS) was obtained on an IS50 spectrometer, before each experiment, the samples were pretreated with N<sub>2</sub> at 300 °C for 1 h and then cooled to the desired temperature. The reaction conditions were set according to the experiment and the full spectrum was recorded in the range of 4000–1000 cm<sup>-1</sup> with a resolution of 4 cm<sup>-1</sup>.

### 2.3. Cells relative viability

After centrifuging 15 mL of sample each time, discarded the supernatant, added 500 μL of 0.01 M PBS phosphate buffer, incubated for 2 h with CCK-8 method, and obtained the OD value of absorbance at a certain wavelength, and calculated the relative viability of cells with Eq. (1).

$$\text{Relative viability of cells(\%)} = \frac{C_a - C_0}{C_b - C_0} \times 100 \quad (1)$$

Where C<sub>a</sub> is mean OD of experimental group, C<sub>b</sub> is mean OD of control group, C<sub>0</sub> is mean OD of blank. The mean OD of blank is the mean value of absorbance of porous plate itself (without culture medium and cells).

## 2.4. Catalytic performance

The catalyst performance testing was carried out in a fixed-bed reactor. 0.1 g of catalyst was weighed and placed in the reaction tube, and the reaction gas was fed into the denitrification reactor through the mass flow meter and gas mixer in turn. The simulated flue gas components were NO<sub>x</sub> concentration of 500 ppm, NH<sub>3</sub> concentration of 500 ppm, O<sub>2</sub> volume fraction of 5%, N<sub>2</sub> as the balance gas, flue gas air velocity was about 32000 h<sup>-1</sup>, and the flue gas flow was controlled at 100 mL/min. The inlet and outlet concentrations of the components were analyzed by an on-line Fourier transform infrared (FTIR) spectrometer (IS50). The NO<sub>x</sub> conversion and N<sub>2</sub> selectivity of the catalysts were calculated using Eqs. (2) and (3).

$$\text{NO}_x \text{ conversion}(\%) = \frac{[\text{NO}_x]_{\text{in}} - [\text{NO}_x]_{\text{out}}}{[\text{NO}_x]_{\text{in}}} \times 100 \quad (2)$$

$$\text{N}_2 \text{ selectivity}(\%) = \left(1 - \frac{2 \times [\text{N}_2\text{O}]_{\text{out}}}{[\text{NO}_x]_{\text{in}} + [\text{NH}_3]_{\text{in}} - [\text{NO}_x]_{\text{out}} - [\text{NH}_3]_{\text{out}}}\right) \times 100 \quad (3)$$

Where [NO<sub>x</sub>] = [NO] + [NO<sub>2</sub>], NO accounts for more than 88%, in and out represent the inlet and outlet of the reactor, respectively.

## 3. Results and discussion

### 3.1. Changes of denitrification activity, cells activity and adsorption mechanism under different synthesis times

#### 3.1.1. Change of denitrification activity

It can be seen from Fig. 1(a) that the concentration of Mn in the centrifugal solution of Chlorella and Mn<sup>2+</sup> mixed for 0–24 h had rapidly decreased in 0.5 h, indicating that the cells and Mn<sup>2+</sup> had the characteristics of rapid binding. Within the time range of 0.5–24 h of mixing, the concentration of Mn in the solution had no significant change, indicating that the combination of the two was stable; It can be seen from Fig. 1(b) that the Chlorella@Mn composite denitrification catalysts prepared at different synthesis times showed different denitrification activities at 75 °C and 175 °C, where the synthesis time refers to the adsorption time of Mn<sup>2+</sup>, the catalyst with synthesis time of 0.5 h had the lowest denitrification activity, after the synthesis time increased to 8 h, the denitrification activity increased slightly, while at 16 h and 20 h, the activity increased rapidly, when the synthesis time was 24 h, the denitrification activity was the highest, and at 175 °C, the NO<sub>x</sub> conversion could reach 98.0%. However, the denitrification activity of 48–120 h synthesis time was close to that of 24 h, indicating that

adequate contact time was required for sufficient reaction between Chlorella cells and Mn<sup>2+</sup>. When reactions were completed, further increase of contact time will no longer promote the improvement of denitrification activity.

Chlorella cells were combined with Mn<sup>2+</sup> at different synthesis times, but the NH<sub>3</sub>-SCR activity was quite different, the specific content of Mn in the catalysts prepared at representative synthesis times (0.5 h, 8 h, 16 h, 24 h, 72 h) was determined by ICP. The results are shown in Table 1, the content of Mn in the catalysts was 51.91–59.13% with relatively small changes, which fully verified that Chlorella cells had combined with a large amount of Mn<sup>2+</sup>. It is noteworthy that different synthesis times exhibit different Mn contents, which may be due to the fact that the adsorption process is dynamic and adsorption and desorption are in relative equilibrium, thus the content of Mn in the catalyst appears to vary slightly at different synthesis times. According to the denitrification activity, it further indicated that the reaction between Chlorella cells and Mn<sup>2+</sup> took a certain time.

#### 3.1.2. Change of cells activity

It can be seen from Fig. S1 that the Chlorella cells used were normal living cells, and almost no death occurred. It was found that after 0.5 h of contact with Mn<sup>2+</sup>, the cells changed from highly dispersed to highly aggregated from Fig. S2, and the state basically remained unchanged with time, when the synthesis time was 0.5 h, Chlorella cells had combined with a large number of Mn<sup>2+</sup>, which is consistent with the above ICP results. We have previously studied mainly electrostatic interaction [28], the adsorption process of Mn<sup>2+</sup> involved electrostatic interaction by Table S1, which was related to the negative groups such as COO<sup>-</sup> and O<sup>-</sup> contained on the cell surface. As can be seen from Fig. S3 and Table S2, the activity of Chlorella cells gradually decreased with increasing synthesis time, and the relative viability of cells decreased from 100.0% to 39.9% in 0 h~8 h, among them, the significant decrease of cells relative viability was in the synthesis time of 0.5 h~8 h, the relative viability of cells decreased 45.7%. Combined with the above analysis results, it was shown that the adsorption of Mn<sup>2+</sup> by Chlorella cells was basically not affected during the process of significant reduction of Chlorella cells activity.

Chlorella is an organism whose cells contain a variety of elements, including K, P, O and other elements. In order to investigate the changes of cells morphology and the distribution of elements (K, P, O, Mn) after adsorption of Mn<sup>2+</sup> by Chlorella cells when the synthesis time reached a relatively stable state within 24 h, TEM was used to test the cells. The results are as shown in Fig. 2, before contact with Mn<sup>2+</sup>, normal Chlorella cells were spherical or oval, and relatively dispersed. In Fig. 2 (a-b), the cells were reunited, and the morphology of the cells changed,

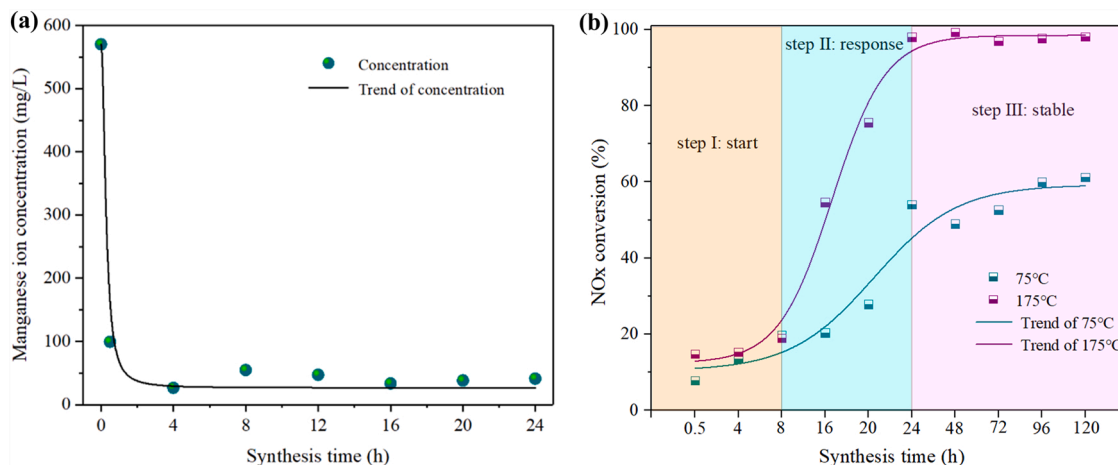
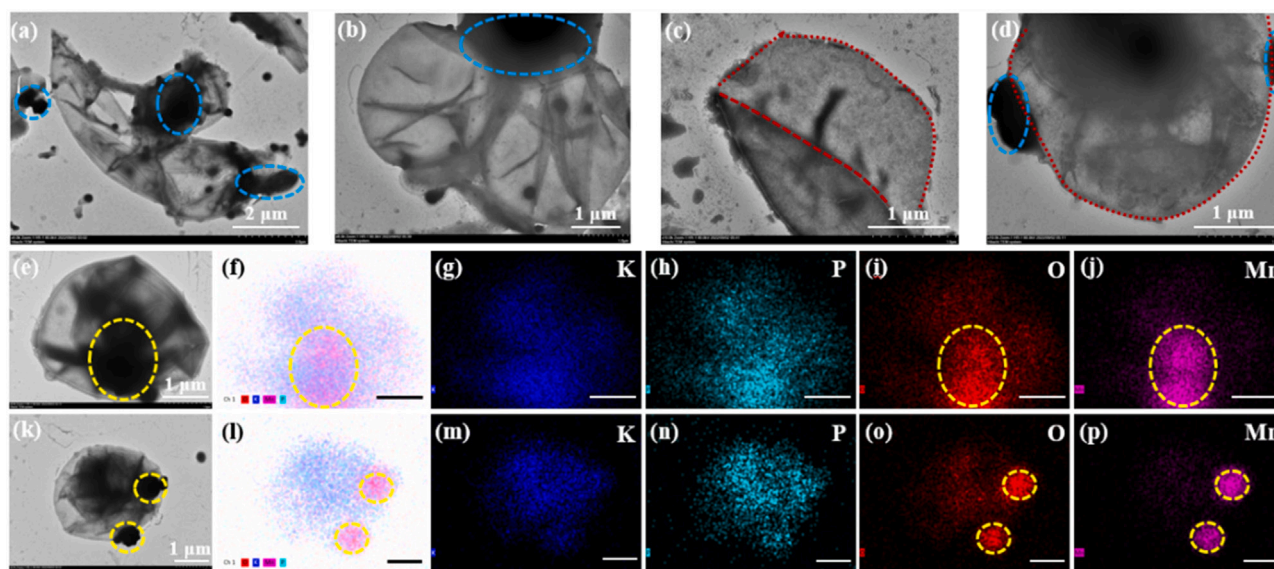


Fig. 1. (a) concentration of manganese ion in centrifuge solution at different synthesis times, (b) NO<sub>x</sub> conversion of the Chlorella@Mn catalyst at 75 °C and 175 °C, reaction conditions: [NO<sub>x</sub>] = [NH<sub>3</sub>] = 500 ppm, [O<sub>2</sub>] = 5 vol.%, balance gas N<sub>2</sub>, GHSV = 32,000 h<sup>-1</sup>.

**Table 1**

Content of Mn in the Chlorella@Mn catalysts with different synthesis times.

Synthesis time (h)	Test-mass (g)	Constant-volume (mL)	Dilution-factor	Specific element	Instrument reading (mg/L)	Conversion of content (mg/kg)	wt%
0.5	0.0337	25	100	Mn	7.3910	548,290.1	54.83
8	0.0327	25	100	Mn	6.8188	521,315.7	52.13
16	0.0298	25	100	Mn	6.1881	519,135.9	51.91
24	0.0632	25	100	Mn	13.584	537,337.8	53.73
72	0.0365	25	100	Mn	8.6332	591,314.4	59.13

Note: Synthesis time refers to the time of  $\text{Mn}^{2+}$  adsorption by Chlorella cells.**Fig. 2.** The TEM images of Chlorella cells adsorbing  $\text{Mn}^{2+}$  for 24 h (a-d) and mapping of K, P, O, Mn elements in a single cell (e-j, k-p).

especially in Fig. 2(a), the original spherical or oval cells were formed into irregular long strips, and the cells were broken. In Fig. 2(c), as shown by the red dotted line, it was found that the cell had obvious plasmolysis, indicating that  $\text{Mn}^{2+}$  was toxic to Chlorella cells, and the change of the final cell state had a greater impact on the cell activity. In Fig. 2(a, b, d), it could also be observed that there were obvious black patches (blue dotted line mark) in the cell, especially on the cell wall. The research showed the adsorption performance of algae to heavy metal ions was mainly determined by the composition and structure of its cell wall [29,30]. The cell wall of algae was generally composed of polysaccharides, proteins and lipids, with a certain negative charge and a large surface area [31]. Algal cell wall components contained a large number of groups that could combine with metal ions, such as carboxyl, amino, amido, carbonyl, hydroxyl, etc. [32,33], these functional groups played an important role in the biological adsorption of metals by algae [34]. Some functional groups could adsorb heavy metal ions through static electricity, and some functional groups had lone pair electrons, which could form coordination bonds with metal ions to adsorb metal ions, ions adsorbed on the surface of some functional groups could exchange with other metal ions [35,36]. The above research showed that the process of algae adsorption of metal ions was a complex physical and chemical process, which was the result of multiple mechanisms.

In the element mapping of a single cell in Fig. 2(e-j), it can be seen that there were more K, P, O and Mn elements in the cell, meanwhile, it was found that the parts with higher concentrations of Mn and O elements were basically consistent (marked with yellow dotted lines), indicating that  $\text{Mn}^{2+}$  mainly combined with and acts on oxygen-containing groups in the process of cell adsorption of  $\text{Mn}^{2+}$ . According to literature research [37,38], the cell wall surface contains a large number of C=O, P=O, O-P-O and other functional groups, it is speculated the above functional groups were related to the adsorption

process of  $\text{Mn}^{2+}$ . Simultaneously, black matter was formed after a large amount of Mn combined with cells, the above phenomenon had also been verified in another single cell in Fig. 2(k-p).

### 3.1.3. FTIR, XRD, XRF

Fourier transform infrared spectroscopy (FTIR) was generally used to determine and analyze the functional groups of materials. In an effort to determine the changes of the functional groups of cells before and after adding  $\text{Mn}^{2+}$  and at different synthetic times, FTIR was carried out. In Fig. 3(a), the peaks of  $3472\text{ cm}^{-1}$  and  $3291\text{ cm}^{-1}$  may be the stretching vibration of surface physically bound water or -OH group [39], and there was no significant change before and after adding Mn. According to the source and peak position distribution of functional groups on the surface of relevant algae materials in Table 2 and the chemistry manual, the peaks of the sample were analyzed.  $2933\text{ cm}^{-1}$  belonged to the stretching vibration of -CH<sub>3</sub> in fatty acids [40,41], after adding Mn, the peak strength decreased, indicating that -CH<sub>3</sub> participated in the adsorption process of Mn.  $1650\text{ cm}^{-1}$  belonged to the stretching vibration peak of amino C=O in algae cells and  $1546\text{ cm}^{-1}$  belonged to the bending vibration peak of amino N-H [42,43], with the extension of Mn addition time, the peak strength decreased, indicating that C=O and N-H also participated in Mn adsorption. The shear vibration peak of  $1459\text{ cm}^{-1}$  which belonged to aliphatic CH<sub>2</sub> changed constantly, indicating that the addition of Mn had an impact on it. The stretching vibration absorption peak at  $1075\text{ cm}^{-1}$  which was attributed to P=O in the cell wall phospholipid, weakens with the increase of time [37], it was more obvious from 16 h to 24 h, indicating that there was a certain reaction between P=O functional group and adsorbed Mn during this period of time, thus affecting the strength of the peak. It was worth noting that 0.5 h after the cells adsorbed  $\text{Mn}^{2+}$ , P=O moved to  $1006\text{ cm}^{-1}$ , due to the role of P containing functional groups and  $\text{Mn}^{2+}$ ,



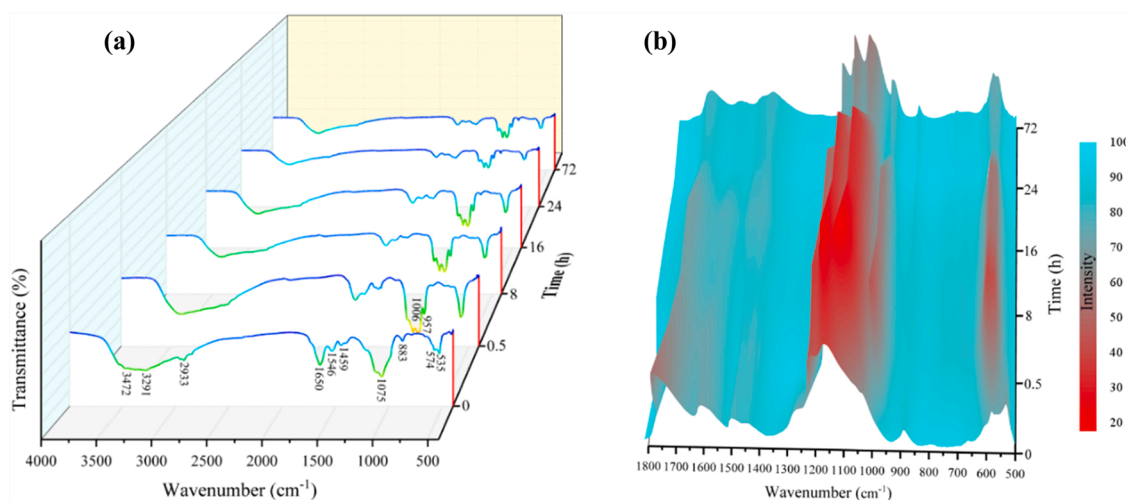


Fig. 3. FTIR spectra (a) and the corresponding 3D mapping results (b) of dried samples at different synthesis times.

Table 2

References of FTIR peak distribution of functional group on the surface of algae.

Wavenumber/ cm <sup>-1</sup>	Functional group	Source	References
3500–3400	-OH	carbohydrate substances	[38,39]
3000–2800/1395	-CH/-CH <sub>2</sub>	aliphatic functional groups	[40,42]
1700–1600	C=O/N-H	carboxylic acids, protein compounds, typical amide	[37,39,42, 43]
1547/1230	-CN	amide, peptide group	[37,40,42]
2918/2854/ 1400–1300	C-H	aliphatic groups	[38,39,42]
2524	S-H	-	[42]
1645/1412/ 1400–1300	COO <sup>-</sup>	carboxylate groups	[39,44,45]
1339/1155/1037	S=O	sulfonyl	[37,38]
1200–1000	C-OH	carboxyl	[39]
1406/1100–1050	P-O	phosphate related groups	[38,39]
1200–900	C-O/C-C/C-O- C/C-O-P	polysaccharides	[40,43,45]
1080	P-O-C/P-O-P/ PO <sub>4</sub> <sup>3-</sup>	-	[40,42]
1253/1240/ 1235/1076/ 1008	P = O	phospholipids, phosphate ester, carbohydrates of nucleic acids	[37,40,42]
1540/852	N-H	proteins	[38,44]
880	P-OR	ester types	[46]
580/545	O-P-O	-	[38]

a weak peak of P-O-P appeared at 957 cm<sup>-1</sup>, the strength of the two peaks also decreased sharply between 16 h and 24 h. 883 cm<sup>-1</sup> was attributed to the bending vibration absorption peak of C-H, after adding Mn, this peak almost disappeared, indicating that C-H played a greater role in the adsorption of Mn. 574 cm<sup>-1</sup> was attributed to the O-P-O vibrational peak [38], which decreased in peak intensity after 0.5 h, decreased significantly between 16 and 24 h, and was already in the weak state at 24 h. The stretching vibrational peak at 535 cm<sup>-1</sup> attributed to N = O, this peak disappeared directly after the addition of Mn, indicating that N = O interacted with Mn, and the above indicated that during the 24 h adsorption reaction of Mn<sup>2+</sup>, the relevant groups were involved in the complexation/chelation of Mn<sup>2+</sup>, in which the oxygen-containing groups played a larger role, which was consistent with the above TEM results. Meanwhile, it was obvious that there was almost no significant change in the spectral curves at 24 h and 72 h, indicating that the interaction between algal cells and Mn reached a steady state after the adsorption time reached 24 h, which was also confirmed with the above NH<sub>3</sub>-SCR results. Fig. 3(b) shows the corresponding 3D mapping results of FTIR spectra at different times, and the

changes of peak intensities with time at each location were further presented, and the results were consistent with the above description, with the reaction time between 0 and 24 h, and the steady state from 24 to 72 h. The main reaction equation occurring during the adsorption process was shown as follow.



Where M represents functional groups of C=O, CH<sub>3</sub>, N = O, C-H, P = O and O-P-O.

In order to determine the changes of crystalline phase of algal cells at different times of Mn<sup>2+</sup> adsorption, XRD is used to analyze the results as shown in Fig. 4(a). When the cells did not adsorb Mn<sup>2+</sup>, the main crystalline species present in the cells were CaHPO<sub>4</sub>·2 H<sub>2</sub>O and CaSO<sub>4</sub>·0.5 H<sub>2</sub>O, and all other components in the cells were amorphous. After Mn<sup>2+</sup> adsorption for 0.5 h, the crystallinity of both species changed, and the peaks disappeared, indicating that the transformation of the crystalline phase may occur on the surface during the adsorption of Mn<sup>2+</sup> by the cells; meanwhile, the peaks of the crystalline species mainly became Mn<sub>3</sub>(PO<sub>4</sub>)<sub>2</sub>·3 H<sub>2</sub>O, indicating the binding of Mn<sup>2+</sup> with P-containing groups, which corresponded to the above FTIR results. While some of the peaks became sharper at 8 h compared with 0.5 h, indicating a further increase in the crystallinity of the species. When the time was increased from 8 h to 16 h, the crystallinity of some of the Mn<sub>3</sub>(PO<sub>4</sub>)<sub>2</sub>·3 H<sub>2</sub>O species decreased and the peak sites of MnCO<sub>3</sub> appeared at 31.1° and 51.3°, respectively, indicating a change in the coordination-bound species of Mn, and more MnCO<sub>3</sub> appeared when 24 h was reached and no major change in the species at 72 h. Combined with the above FTIR and XRD results, it indicated that from 0.5 h to 16 h, the Mn<sup>2+</sup> and related functional groups were in a slow reaction state, and from 16 h to 24 h, a more intense reaction occurred between species, and after 24 h, the species interactions in the cells weakened and entered a relatively stable state.

To determine the changes in the content of alkali metals (K, Na) and alkaline earth metals (Ca, Mg) in the catalyst between 0.5 h and 24 h of synthesis time, XRF was performed, and the results are shown in Fig. 4 (b). Ca decreased from 2.10% to 0.53%, K decreased from 1.34% to 0.97%, and Mg decreased from 0.49% to 0.36%, indicating that the contents of Ca, K, and Mg all decreased to varying degrees with increasing synthesis time, while Na increased from 0.31% to 0.91%, which may be due to the adsorption of Na<sup>+</sup> in culture solution by the cells. The above indicated that the ion exchange mechanism occurred during the adsorption of Mn<sup>2+</sup> by the cells, in which the exchanged metal cations were mainly Ca<sup>2+</sup>, K<sup>+</sup>, Mg<sup>2+</sup>, and the ion exchange process may occur gradually with the increase of time, the order of the ion exchange amount by calculating the decrease percentage of Ca, K and Mg

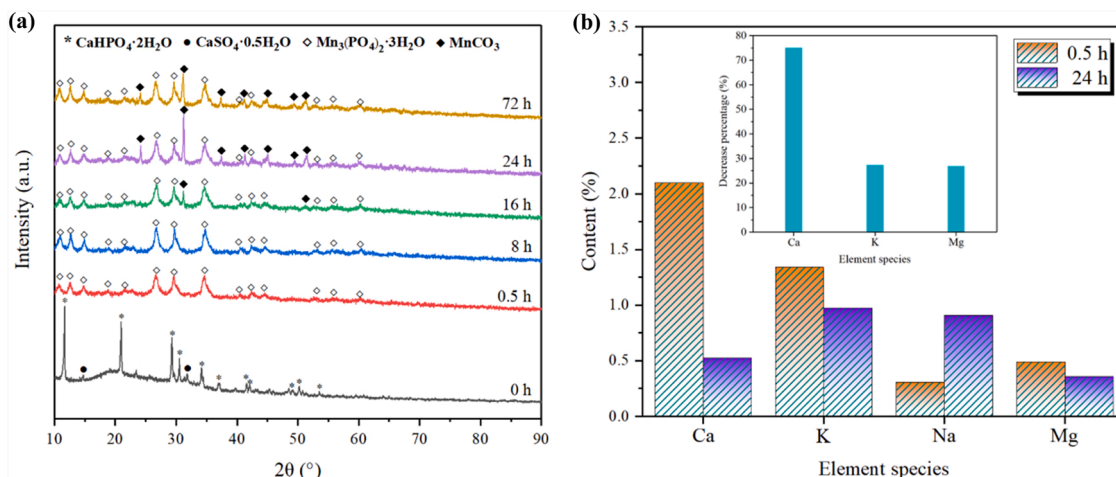


Fig. 4. XRD patterns of dried samples at different synthesis times (a), Ca, K, Na, Mg content of Chlorella@Mn catalysts at 0.5 h and 24 h synthesis time (b).

was most likely:  $\text{Ca}^{2+} > \text{K}^+ > \text{Mg}^{2+}$ .

### 3.1.4. Adsorption mechanism

Through the above correlation analysis, a schematic diagram of the mechanism of  $\text{Mn}^{2+}$  adsorption by Chlorella cells in water was obtained as shown in Fig. 5, the whole adsorption process was a complex physicochemical process, in which there were three main adsorption mechanisms, namely ion exchange, complexation/chelation and electrostatic interaction.  $\text{Mn}^{2+}$  mainly occurred with  $\text{Ca}^{2+}$ ,  $\text{K}^+$ , and  $\text{Mg}^{2+}$  during ion exchange, and the corresponding exchange capacity was speculated to be  $\text{Ca}^{2+} > \text{K}^+ > \text{Mg}^{2+}$ . Complexation/chelation was mainly  $\text{C}=\text{O}$ ,  $-\text{CH}_3$ ,  $\text{N}=\text{O}$ ,  $\text{C}-\text{H}$ ,  $\text{P}=\text{O}$  and  $\text{O}-\text{P}-\text{O}$  functional groups interact with  $\text{Mn}^{2+}$ ,  $\text{Mn}^{2+}$  and related functional groups were in a slow reaction state in 0.5 h~16 h, and at 16 h~24 h, violent reaction occurred between the species, and after 24 h, the reaction was completed and reached a relatively stable state. Electrostatic interaction occurred mainly between  $\text{O}^-$ ,  $\text{COO}^-$  and other negatively charged groups on the cell wall surface and the positively charged  $\text{Mn}^{2+}$  to neutralize the charge, electrostatic interaction process was rapid, the state of Chlorella cells had changed significantly when adding  $\text{Mn}^{2+}$  for 0.5 h, and the cells had changed from a highly dispersed state to a highly agglomerated state. The above three processes occurred when Chlorella cells first came into contact with  $\text{Mn}^{2+}$ , with the ion exchange and complexation/chelation processes in particular showing significant timeliness, the reaction process

was gradually completed as the synthesis time increased.

## 3.2. Physicochemical characteristics and denitrification activity of stable catalyst

### 3.2.1. XRD and UV-vis DRS

The catalysts obtained after calcination of the samples at different synthesis times were tested separately by XRD to determine the effect of different synthesis times on the crystalline phase. As can be seen in Fig. 6 (a), there were no sharp peak pattern, low crystallinity and few peaks at different synthesis times, indicating that the active ingredients exist mainly in the amorphous form, and at 0.5 h, the crystalline phases of  $\text{K}_2\text{O}$  and  $\text{CaO}$  appear at  $29.4^\circ$  and  $31.9^\circ$  respectively. While weak peaks of  $\text{NaPO}_3$  species appear at  $17.5^\circ$ , and when the time increased to 24 h, the  $\text{K}_2\text{O}$  and  $\text{CaO}$  peaks both disappeared and  $\text{K}_2\text{SO}_4$  species appeared at  $30.1^\circ$  and became the main crystalline phase species,  $\text{MgSiO}_3$  species appeared at  $36.8^\circ$ , and the  $\text{NaPO}_3$  peak intensity further increased, indicating crystallinity was further improved. It was speculated that the disappearance of  $\text{K}_2\text{O}$  and  $\text{CaO}$  and the formation of  $\text{K}_2\text{SO}_4$  and  $\text{MgSiO}_3$  will enable the active site to normally play the role of denitrification, thus showing a significant increase in  $\text{NH}_3$ -SCR activity, indicating that  $\text{K}_2\text{O}$  and  $\text{CaO}$  had seriously affected the denitrification activity of the catalyst during 0.5–16 h synthesis time. Notably, no obvious peaks of  $\text{MnO}_x$  species were found, combining the above FTIR and XRD results, it is speculated that a part of Mn may exist in the form of amorphous metal oxides, especially  $\text{MnO}_x$ , and the remaining part of Mn is bonded to functional groups, especially between Mn and  $\text{P}=\text{O}$ ,  $\text{C}=\text{O}$ , etc., thus Mn exists in different forms in the Chlorella@Mn catalyst. Here, it should be mentioned that because Chlorella is a living organism, the XRD results of Chlorella@Mn catalysts prepared under the same conditions each time will also have certain differences.

To further elucidate the structural differences between the catalysts with synthesis times of 0.5 h and 24 h, UV-vis DRS was characterized, as shown in Fig. 6 (b), both the Chlorella and Chlorella@Mn catalysts had wide absorption bands in the range of 200–400 nm, where Chlorella exhibited strong UV absorption with a steep spectrum at the absorption edge around 350 nm, indicating that the UV absorption was caused by the band gap transition, the absorption peak near 240 nm can be considered as  $\text{P}-\text{O}$  charge transfer transition, 24 h had a relatively stronger absorption peak at 235 nm compared to 0.5 h, indicating a higher number of  $\text{P}-\text{O}$  functional groups on its surface, while the absorption peak at 291 nm was attributed to  $\text{C}=\text{O}$  or  $\text{N}=\text{N}$ , and absorption peak was stronger in Chlorella, indicating that the associated functional groups were more. While the addition of Mn changed the surface amount of some functional groups in Chlorella, and the absorption peak at 664 nm attributed to octahedral coordination of  $\text{MnO}_2$ ,

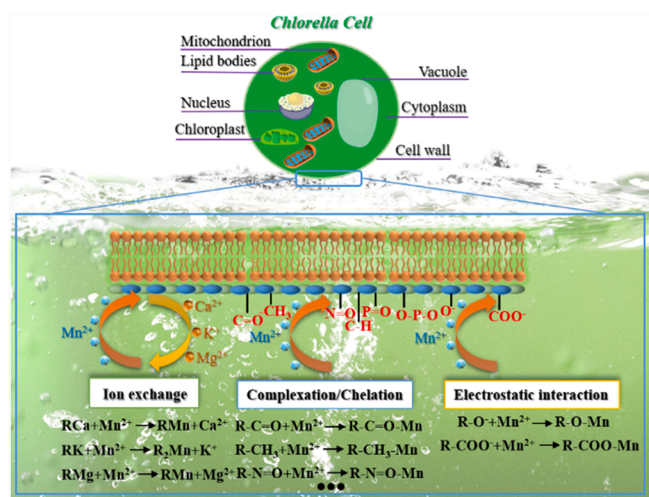


Fig. 5. Schematic diagram of adsorption mechanism of Chlorella cell to  $\text{Mn}^{2+}$  in water.

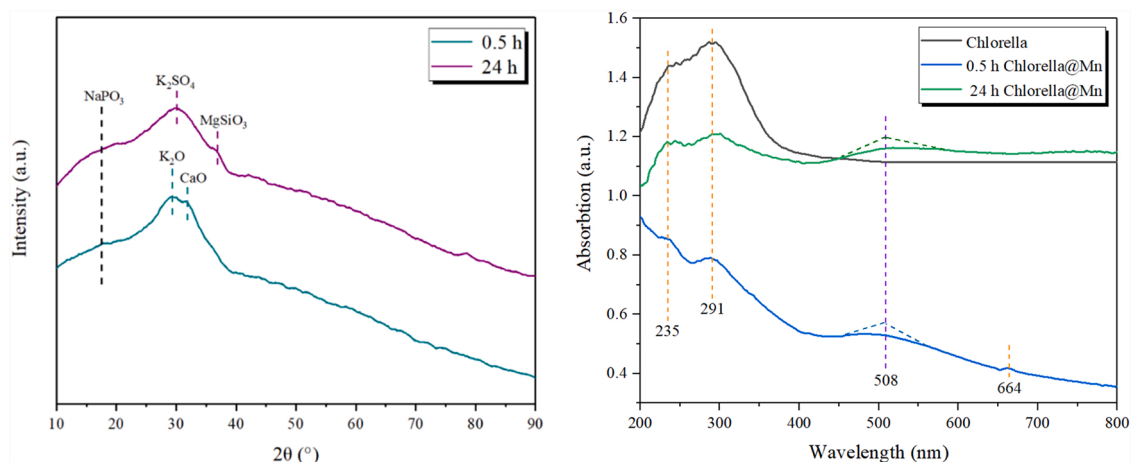


Fig. 6. XRD patterns of Chlorella@Mn catalysts at different synthesis times (a), Chlorella and Chlorella@Mn catalysts: UV-vis DRS spectra (b).

indicating the presence of a certain amount of  $\text{MnO}_2$  species on the catalyst surface at the synthesis time of 0.5 h. While at 450–600 nm, Chlorella@Mn had higher UV absorption due to the presence of MnOx with narrow band gap, which broadened the UV absorption range of the catalyst. The shoulder at 508 nm belonged to the d-d electron leap in  $\text{Mn}^{3+}$  and  $\text{Mn}^{4+}$ , indicating that Mn was present in the multivalent form in Chlorella@Mn. It was noteworthy that the synthesis time of 24 h compared to 0.5 h was stronger in the peak here, combined with XRD, which was presumed to be due to the influence of  $\text{K}_2\text{O}$  and CaO present on the surface, indicating that the catalyst surface synthesized at 24 h possessed more MnOx species, which was conducive to the charge transfer in SCR reaction, thus leading to higher catalytic activity.

### 3.2.2. XPS

To determine the valence changes of the main elements Mn, P and O in the Chlorella@Mn catalyst at different synthesis times, XPS was used to test respectively. We previously carried out a study of XPS results for a synthesis time of 24 h [28], here, 0.5 h is compared with 24 h. Fig. 7(a), when the synthesis time was 0.5 h, the Mn2p spectrum showed that catalyst contained  $\text{Mn}^{4+}$  (643.7 eV),  $\text{Mn}^{3+}$  (642.1 eV) and  $\text{Mn}^{2+}$  (641.1 eV) [47,48], where  $\text{Mn}^{3+}/(\text{Mn}^{4+} + \text{Mn}^{3+} + \text{Mn}^{2+})$  was 25%. As the synthesis time increased from 0.5 h to 24 h, the content of  $\text{Mn}^{3+}$  changed greatly, increasing to 47%, indicating that the coordination environment of Mn changed between 0.5 h and 24 h, eventually contributing to the higher content of  $\text{Mn}^{3+}$  valence state when the time was 24 h. According to literature research [49,50], the high presence of

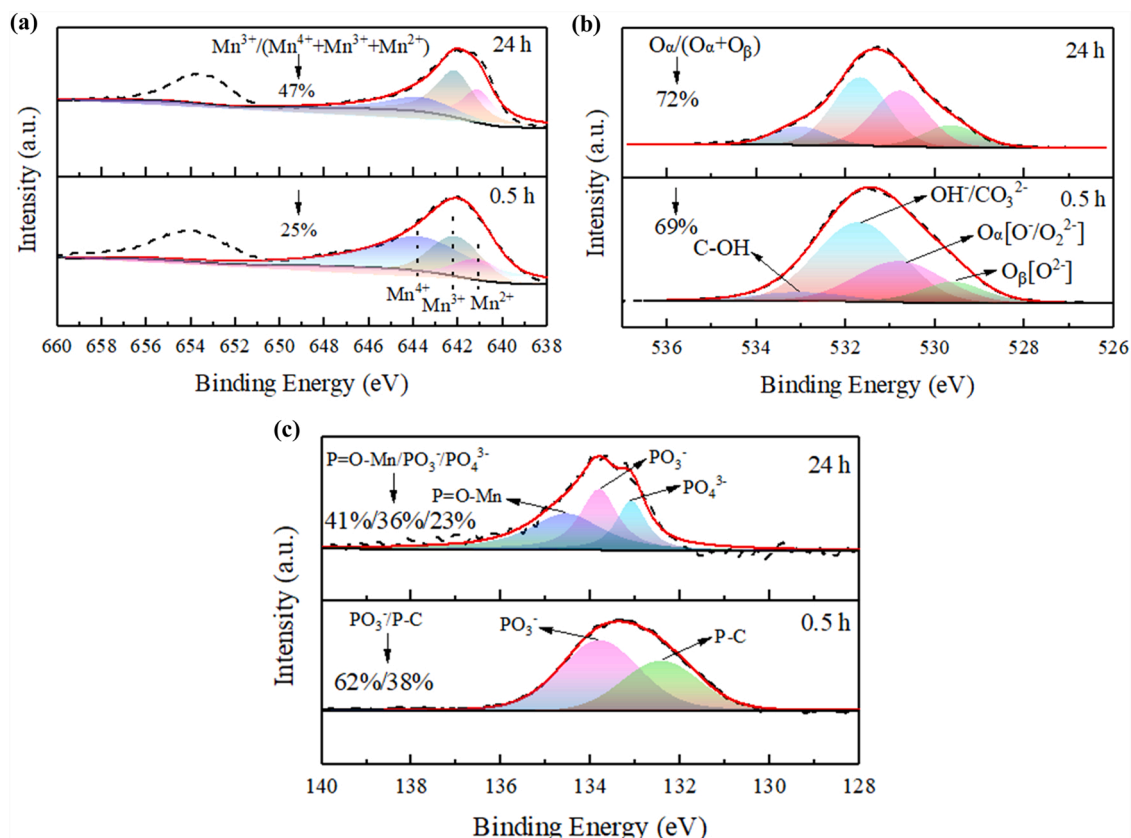


Fig. 7. XPS spectra of Chlorella@Mn catalysts at different synthesis times: Mn2p (a), O1s (b), P2p (c).



Mn<sup>3+</sup> was beneficial to improve activity of NH<sub>3</sub>-SCR reaction.

Fig. 7(b), the O1s spectrum at 0.5 h indicated that the catalyst contained C-OH (533.0 eV), OH/CO<sub>3</sub><sup>2-</sup> (531.7 eV), surface chemisorbed oxygen O<sub>α</sub> [O<sup>2</sup>/O<sub>2</sub><sup>2-</sup> (530.8 eV)] and lattice oxygen O<sub>β</sub> [O<sup>2-</sup> (529.6 eV)] [51,52], where O<sub>α</sub>/(O<sub>α</sub> + O<sub>β</sub>) was 69%. The content of O<sub>α</sub> increased to 72% when the synthesis time was increased to 24 h, indicating that the catalyst surface composition varied considerably during the time period from 0.5 h to 24 h. The 24 h was more favorable for O<sub>2</sub> adsorption and activation, prompting a large amount of O<sub>α</sub> production. The surface chemisorbed oxygen had a high mobility, which enabled the rapid replenishment of active oxygen molecules in the NH<sub>3</sub>-SCR reaction, thus ensuring the smooth progress of efficient denitrification reaction [53, 54].

Phosphorus was a component element of many functional groups in Chlorella cells, and it was clear from the above FTIR results that P-containing groups were involved in the adsorption process of Mn<sup>2+</sup>, where the valence change process regarding P in the catalysts prepared at different adsorption times is shown in Fig. 7(c). At 0.5 h, XPS showed the presence of PO<sub>3</sub> and P-C species at 133.8 eV, 132.4 eV, respectively [55], with the percentage of content of 62% and 38%, respectively. As the time increased from 0.5 h to 24 h, the content of PO<sub>3</sub> was greatly reduced and the peak of P-C disappeared, simultaneous, new peaks appeared, including P = O-Mn (134.5 eV, 41%) and PO<sub>4</sub><sup>3-</sup> (133.1 eV, 23%) [56]. The above indicated that the ligand environment of P changed dynamically at different times, the appearance of P = O-Mn was consistent with the FTIR and SEM results, indicating that a deep reaction between P = O and Mn during 0.5 h~24 h, and finally there were a large number of P = O-Mn groups on the catalyst surface. It was possible that some of the PO<sub>3</sub> were converted to PO<sub>4</sub><sup>3-</sup> due to electron transfer between PO<sub>3</sub> and Mn, the production of PO<sub>4</sub><sup>3-</sup> may have further enhanced the acidity of the Chlorella@Mn catalyst, thus making it more favourable for NH<sub>3</sub> adsorption and activation, ultimately further improving the NH<sub>3</sub>-SCR activity.

### 3.2.3. FTIR and BET

As can be seen from Fig. 8, the Chlorella@Mn catalyst with synthesis time of 24 h showed stretching vibration of surface physically bound water or -OH groups in the FTIR spectra before and after calcination, with peaks at about 3400 cm<sup>-1</sup> [44,46]. 1636 cm<sup>-1</sup> was attributed to the C=O stretching vibration peak, 1532 and 861 cm<sup>-1</sup> were the N-H stretching vibration peak, and 1125 cm<sup>-1</sup> was classified as the C-O-C symmetric stretching vibration peak [45], and all of the above peaks appeared to be weakened under calcination at 450 °C, where the N-H and C-O-C peaks almost disappeared, indicating serious volatilization of N-H and C-O-C. Notably, the peak intensities of P-containing functional groups including P = O asymmetric stretching vibration (1013 cm<sup>-1</sup>), P-O-P symmetric stretching vibration (952 cm<sup>-1</sup>) and O-P-O vibrational peaks (582 cm<sup>-1</sup>) also disappeared after calcination treatment,

indicating that the coordination state of P also changed with the volatilization of most of the species. P-O stretching vibration (1405 cm<sup>-1</sup>) and P = O stretching vibration (1066 cm<sup>-1</sup>) peaks weakened but did not disappear, indicating the presence of a certain number of P-O and P = O functional groups on the Chlorella@Mn catalyst surface after calcination. Meanwhile, the symmetric stretching vibrational peak of Mn-O (561 cm<sup>-1</sup>) appeared after calcination [57], indicating the generation of MnOx species on the catalyst surface. Meanwhile, in our previous study [28], through N<sub>2</sub> adsorption-desorption isotherms (Fig. S4, Table S3), Chlorella@Mn catalyst before calcination exhibited type III adsorption isotherms, it was found that the calcined Chlorella@Mn catalyst formed type IV adsorption isotherms and H3 type hysteresis loops with a pore size of 3.8 nm, belonging to a mesoporous structure. The specific surface area of the Chlorella@Mn after calcination was 122 m<sup>2</sup>/g, which was much larger than the value of 27 m<sup>2</sup>/g for the Chlorella@Mn before calcination, indicating that the calcination treatment increased the specific surface area of the catalyst to some extent.

### 3.2.4. Denitrification performance and SO<sub>2</sub>, H<sub>2</sub>O poisoning resistance

The above FTIR, XRD and XPS analyses show that the reaction intensities among the Mn<sup>2+</sup> and related functional groups were different at different synthesis times, and the corresponding relationship between the interspecies action intensities and NOx conversion is shown in Fig. 9 (a). Within the time range of 0.5–16 h, the relevant species were in a slow reaction state, and the NOx conversion reached the highest 54.6% at 16 h, and the state changed significantly during the period of 16–24 h, in which violent reaction occurred, while finally it was in a basically stable state after 24 h, the NOx conversion was as high as 98.0% at 24 h and also stable at 97.0% at 72 h.

In our previous study [28], it was found that Chlorella@Mn catalyst possessed stronger low-temperature redox performance compared with the MnOx catalyst by H<sub>2</sub>-TPR (Fig. S5), the NH<sub>3</sub>-SCR activity results of the Chlorella@Mn and MnOx catalysts were shown in Fig. S6(a), Chlorella@Mn showed higher NOx conversion and N<sub>2</sub> selectivity compared with the MnOx catalyst at 100–225 °C, NOx conversion was close to 100%, indicating its better low-temperature catalytic performance. Meanwhile, it can be seen from Fig. S6(b) that Chlorella@Mn catalyst has better long-term denitrification stability than the MnOx catalyst at 200 °C. It can be seen from Fig. S6(c) that Chlorella@Mn catalyst can delay the poisoning caused by SO<sub>2</sub> compared with the MnOx catalyst at 175 °C and 150 ppm SO<sub>2</sub> [28], but the denitrification activity was also very low after 10 h, and the NH<sub>3</sub>-SCR activity was reduced to about 35%. After SO<sub>2</sub> was removed, the activity was not recovered. In the future, it is necessary to improve the anti-SO<sub>2</sub> poisoning performance of Chlorella@Mn catalyst by surface modification or element doping, etc.

It was found by Fig. 9(b) that at 200 °C, when 8 vol.% H<sub>2</sub>O was just passed, the SCR activity of both catalysts decreased significantly, but the

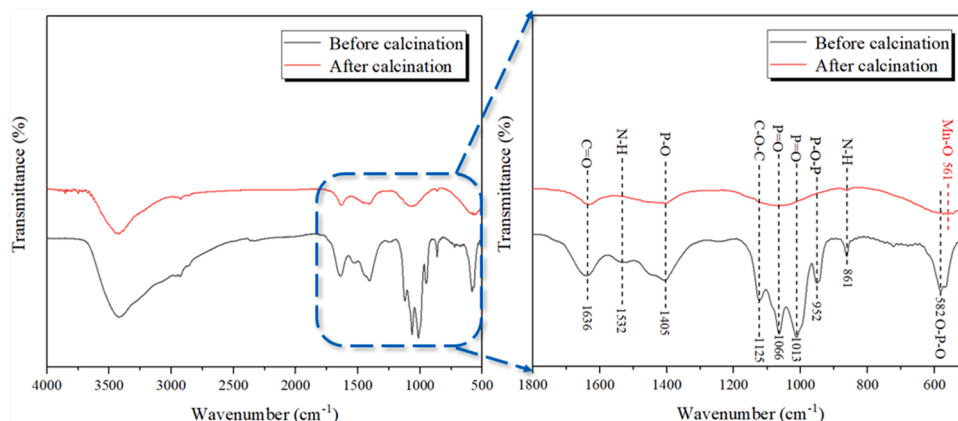
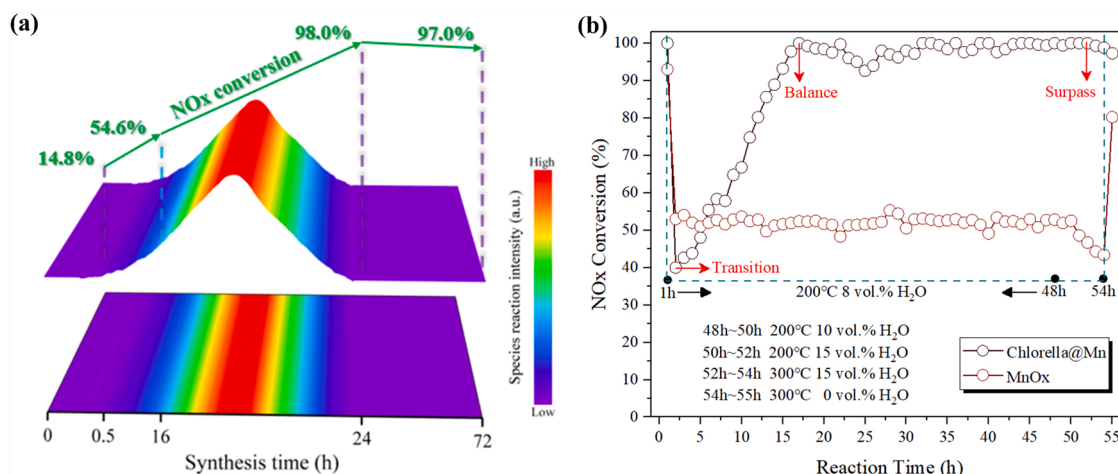


Fig. 8. Chlorella@Mn catalyst: FTIR spectra before and after calcination.





**Fig. 9.** (a) Schematic diagram of species reaction intensity and NO<sub>x</sub> conversion at different synthesis times; (b) NO<sub>x</sub> conversion of the Chlorella@Mn and MnO<sub>x</sub> catalysts at 200–300 °C: H<sub>2</sub>O resistance. Reaction conditions: [NO<sub>x</sub>] = [NH<sub>3</sub>] = 500 ppm, [O<sub>2</sub>] = 5 vol.%, [H<sub>2</sub>O] = 8–15 vol.% (when used), balance gas N<sub>2</sub>, GHSV = 32,000 h<sup>-1</sup>.

SCR activity of the Chlorella@Mn catalyst decreased more significantly than the MnO<sub>x</sub> catalyst, it is speculated that this is because the competitive adsorption of H<sub>2</sub>O and the reaction gases is stronger at the beginning of the contact with H<sub>2</sub>O, therefore, the toxic effect on the Chlorella@Mn catalyst is greater than the MnO<sub>x</sub> catalyst. However, the activity of Chlorella@Mn turned around after 1 h of passing water and the activity started to recover gradually, which may be due to the dissociation and activation of H<sub>2</sub>O on the catalyst surface when H<sub>2</sub>O reached a certain concentration, generating a large number of hydroxyl groups, increasing the proportion of reactive oxygen species on the surface or forming Brønsted acid sites which enhanced the adsorption and activation of NH<sub>3</sub>, thus allowing denitrification performance to recover gradually. At 16 h after passing water, the activity was completely restored, indicating that the toxic effect of H<sub>2</sub>O reached a dynamic balance with the dissociation and activation effects, so that H<sub>2</sub>O no longer had a negative effect on the NH<sub>3</sub>-SCR reaction. In 48 h~54 h, the reaction was more stable when 10% and 15% of H<sub>2</sub>O were passed in turn and the reaction temperature was increased to 300 °C, and denitrification activity was all high. SCR activity was basically unchanged after removing H<sub>2</sub>O, while SCR activity of the MnO<sub>x</sub> catalyst was lower in the presence of H<sub>2</sub>O, and NO<sub>x</sub> conversion only floated around 50%. The above indicated that Chlorella@Mn had better H<sub>2</sub>O poisoning resistance performance than the MnO<sub>x</sub> catalyst, the dissociation and activation effect of H<sub>2</sub>O may surpass the toxicity effect at 52 h, which made the Chlorella@Mn catalyst maintain higher NH<sub>3</sub>-SCR activity at 300 °C. At the same time, compared with conventional

denitrification catalysts (Table 3), Chlorella@Mn catalyst has excellent H<sub>2</sub>O poisoning resistance, which makes it more conducive to industrial application. Meanwhile, it is worth mentioning that compared with the SCR catalysts preparation methods in Table 3, the biological method in this paper has the advantages of simple preparation process and high preparation efficiency, etc.

### 3.2.5. SEM-EDS

To determine the morphology and elemental distribution of the Chlorella@Mn catalyst at 24 h steady state, SEM-EDS were carried out, and the results were shown in Figs. 10 and 11, where it can be seen from Fig. 10(a-e) that the catalyst was in a state of interleaved distribution of lamellae and particles, with some of the particles (marked by red circles) being semi wrapped by the nanoscale lamellae structure, the presence of lamellae structure may contribute to the relatively high specific surface area, which was conducive to the adsorption of reaction species and the mass transfer of reactants/products [63], thus allowing the NH<sub>3</sub>-SCR reaction to proceed smoothly. From Fig. 10(f-s), the elements were relatively uniformly distributed on the catalyst surface, and it was worth noting that the distribution trends of different elements were different, and the positions of the wireframe markers in each EDS mapping map further indicated different distribution states among the elements, among which, C, N, and O elements had high distribution similarity, P and organic elements also had some similar distribution among them, while the distribution of Na and P was highly consistent, and it was presumed that the coordination structure was formed between Na and P.

**Table 3**

Comparison of H<sub>2</sub>O poisoning resistance between Chlorella@Mn catalyst and conventional denitrification catalysts.

Catalyst	Preparation method	Reaction conditions	NO <sub>x</sub> conversion	Reference
Mn-Ce/TiO <sub>2</sub>	Incipient wetness impregnation	500 ppm NO, 500 ppm NH <sub>3</sub> , 5 vol% O <sub>2</sub> , <b>3 vol.% H<sub>2</sub>O</b> , N <sub>2</sub> balance, 200 °C, GHSV = 60,000 h <sup>-1</sup>	35%	[58]
Mn/ACN	One-step wet impregnation	1000 ppm NO, 1000 ppm NH <sub>3</sub> , 5 vol% O <sub>2</sub> , <b>10 vol.% H<sub>2</sub>O</b> , He balance, 175 °C, GHSV= 18,000 h <sup>-1</sup>	Approximately 56%	[23]
Fe-Mn/SBA-15	One-step incipient wetness impregnation	300 ppm NO, 300 ppm NH <sub>3</sub> , 3 vol% O <sub>2</sub> , <b>5 vol.% H<sub>2</sub>O</b> , 200 °C	80%	[59]
Zr-Mn/Raw biochar	Impregnation	500 ppm NO, 500 ppm NH <sub>3</sub> , 5% O <sub>2</sub> , <b>5% H<sub>2</sub>O</b> , N <sub>2</sub> balance, 200 °C, GHSV= 36,000 h <sup>-1</sup>	66%	[60]
MnFeW/Ti	Ultrasonic-assisted impregnation	500 ppm NH <sub>3</sub> , 500 ppm NO, 5% O <sub>2</sub> , <b>5 vol.% H<sub>2</sub>O</b> , N <sub>2</sub> balance, GHSV = 80,000 h <sup>-1</sup>	Approximately 95%	[61]
Mn/Ce	Hydrothermal	500 ppm NO, 500 ppm NH <sub>3</sub> , 3 vol% O <sub>2</sub> , <b>5 vol.% H<sub>2</sub>O</b> , N <sub>2</sub> balance, 150 °C, GHSV= 52,500 h <sup>-1</sup>	Approximately 78%	[62]
NiMn	Glycine combustion	600 ppm NO, 600 ppm NH <sub>3</sub> , 5 vol% O <sub>2</sub> , <b>10 vol.% H<sub>2</sub>O</b> , N <sub>2</sub> balance, 90 °C, GHSV= 45,000 h <sup>-1</sup>	Approximately 83%	[48]
Chlorella@Mn	Biosorption	500 ppm NO, 500 ppm NH <sub>3</sub> , 5 vol% O <sub>2</sub> , <b>8–15 vol.% H<sub>2</sub>O</b> , N <sub>2</sub> balance, 200–300 °C, GHSV= 32,000 h <sup>-1</sup>	Approximately 100%	This paper

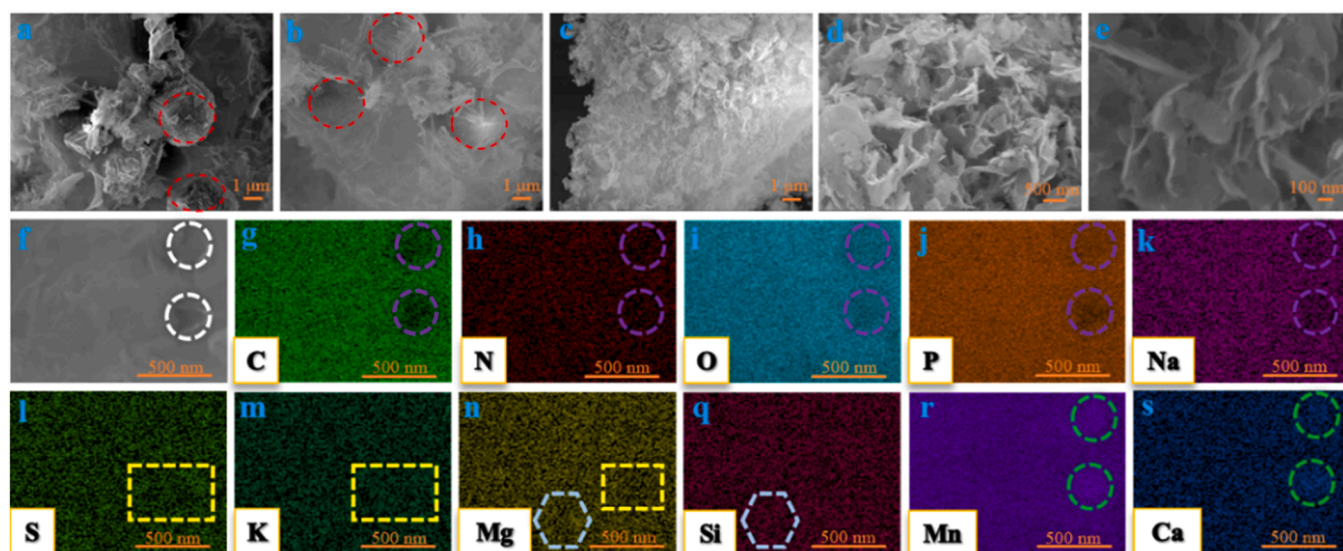


**Fig. 10.** SEM images of Chlorella@Mn catalyst at different magnifications: (a-c) 1  $\mu\text{m}$ , (d) 500 nm, (e) 100 nm, (f) 500 nm, and EDS mapping images: (g) C, (h) N, (i) O, (j) P, (k) Na, (l) S, (m) K, (n) Mg, (q) Si, (r) Mn, (s) Ca.

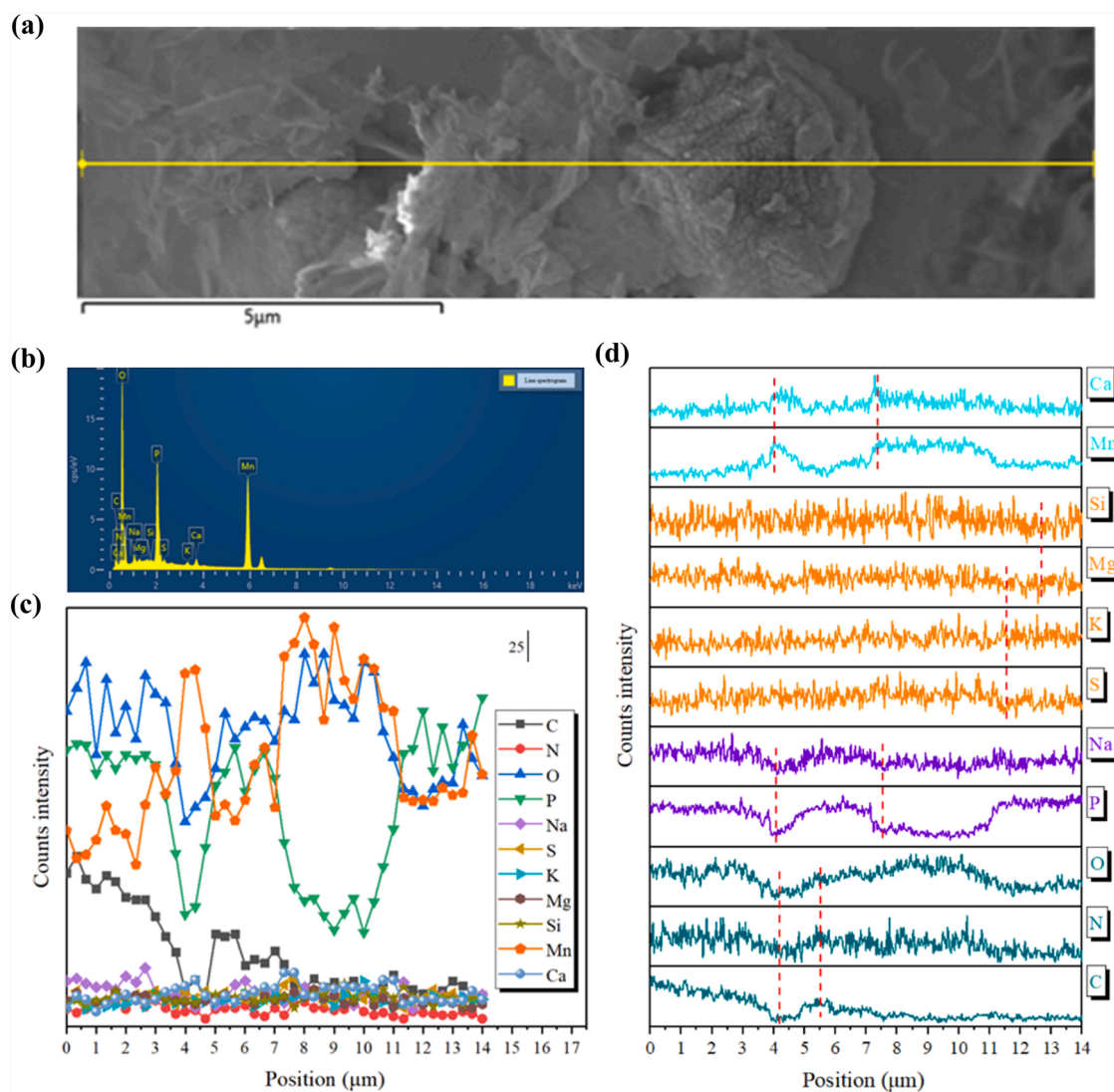


**Fig. 11.** SEM-EDS line scanning results of the Chlorella@Mn catalyst: (a) SEM image; (b) Line spectrogram; (c-d) Line scanning data of elemental distribution.

The distribution states of K and S elements were basically consistent, meanwhile, in the distribution of Mg elements, it was found that some Mg and S had the same distribution state, and other Mg and Si elements had the same distribution, the above indicated that the coordination structure was more likely to be formed between K and S, Mg and S, Mg and Si through bonding, which was also consistent with the above XRD results, further suggesting the presence of acid-base neutralization phenomenon on the catalyst surface; unexpectedly, the distribution of Ca was correlated with the element Mn, and usually the presence of Ca affected activity of the Mn-O site, leading to reduced denitrification performance, but in this study, the catalyst had high SCR activity, indicating that the presence of Ca may play a positive role, presumably in the form of amorphous  $\text{Ca}_x\text{Mn}_y\text{O}_z$  presences on the surface of Chlorella@Mn catalyst.

From the linear scanning and energy spectrum in Fig. 11(a-c), it was clear that Mn, O and P were the main elements of catalyst, it was further found that the lamellar composition was mainly P, O, Mn, based on the above analysis, it may be a bonding species between  $\text{P}=\text{O}$  and Mn. The granular composition was mainly O, Mn, and more likely  $\text{MnO}_x$  species. The line scan results of each element in Fig. 11(d), especially where the red dashed line marks, further verified the above speculation. Different alkali metals (K, Na) and alkaline earth metals (Ca, Mg) had different coordination structures on the catalyst surface, and their coordination information had a greater correlation with  $\text{NH}_3$ -SCR activity in combination with the above characterization and analysis, in which the presence of P, S, Si three elements formed acid species greatly reduced toxicity of Na, K and Mg to Chlorella@Mn catalyst, thus protecting the active sites on the catalyst surface from the poisoning of Na, K and Mg

related species; meanwhile, the distribution state between Ca and Mn was almost same, which again indicated the combination of Ca and Mn, and the above good coordination state guaranteed effective operation of active sites, which finally led Chlorella@Mn catalyst to avoid poisoning caused by alkali/alkaline earth metal, thus ensuring a high low-temperature denitrification activity. Combined with the above characterization and analysis results, it is shown that the presence of  $\text{PO}_3^-$ ,  $\text{SO}_4^{2-}$  and  $\text{SiO}_3^{2-}$  on the catalyst surface may help to improve the resistance to alkali/alkaline earth metal poisoning of the Chlorella@Mn catalyst.

### 3.2.6. In-situ DRIFTS

The adsorbed species of  $\text{NO}+\text{O}_2$  on the surface of the  $\text{MnO}_x$  and Chlorella@Mn catalysts were analyzed by in-situ DRIFTS, respectively. As shown in Fig. 12(a, a1), at the adsorption time of 20 min, the  $\text{MnO}_x$  catalyst surface generated bridged nitrate ( $1245\text{ cm}^{-1}$ ), monodentate nitrite ( $1379\text{ cm}^{-1}$ ), monodentate nitrate ( $1470\text{ cm}^{-1}$ ), bidentate nitrate ( $1541\text{ cm}^{-1}$ ), adsorbed  $\text{NO}_2$  ( $1628\text{ cm}^{-1}$ ), and chemisorbed NO ( $1743\text{ cm}^{-1}$ ) species [64,65], the peak strength increased with the increase of time from 1 to 20 min, indicating an increase in adsorption. In Fig. 12(b, b1), monodentate nitrate ( $1294\text{ cm}^{-1}$ ), bidentate nitrate ( $1538\text{ cm}^{-1}$ ), chemisorbed NO ( $1743\text{ cm}^{-1}$ ), and weakly adsorbed NO ( $1829\text{ cm}^{-1}$ ) species appeared on the surface of Chlorella@Mn catalyst, respectively. It was worth noting that Chlorella@Mn contained a higher content of monodentate nitrate than  $\text{MnO}_x$  catalyst, which may be formed after NO was adsorbed and activated on the  $\text{P}=\text{O}$ -Mn structural sites. The comparison revealed more nitrate on the surface of Chlorella@Mn, indicating stronger adsorption of NO. Meanwhile, more  $\text{NO}_2$

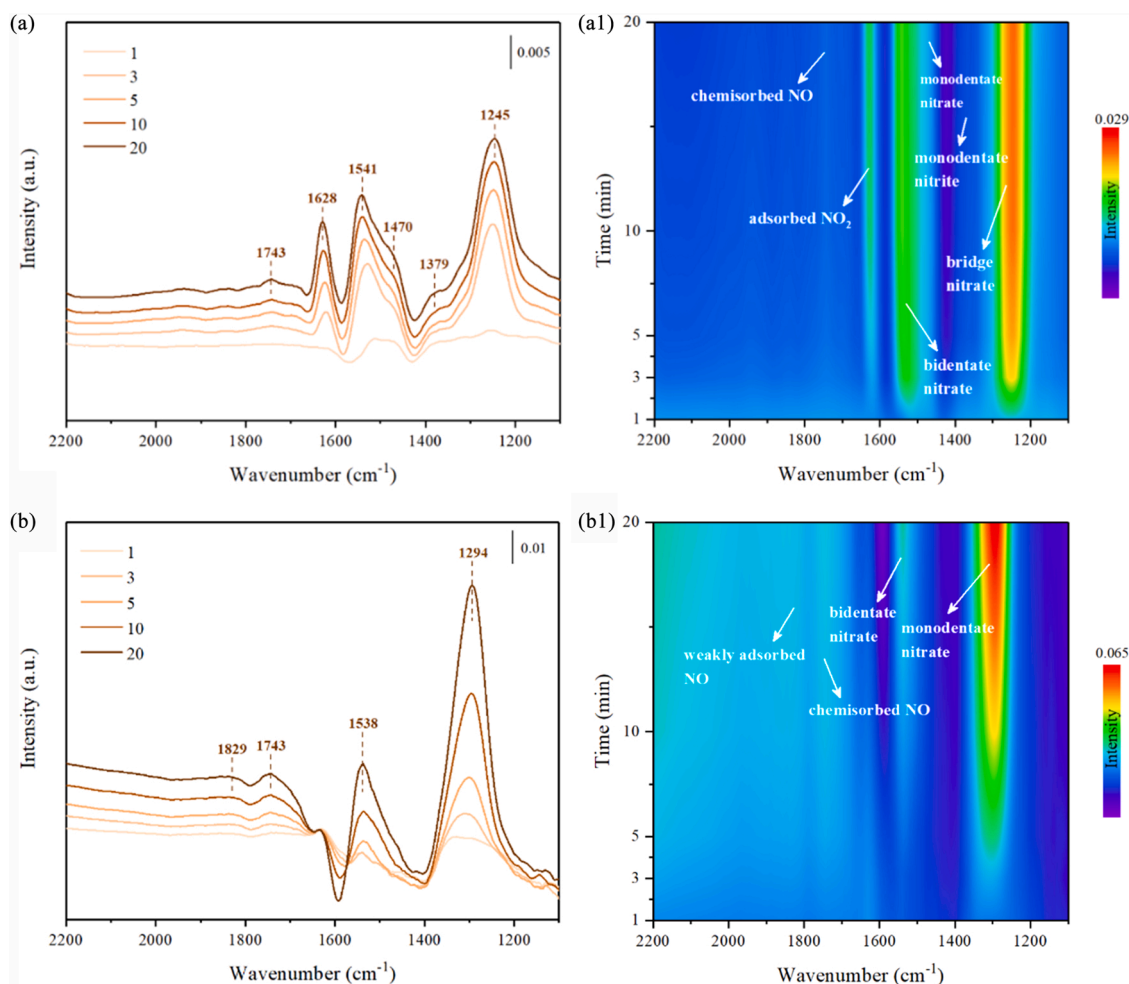


Fig. 12. In-situ DRIFT spectra for the adsorption of  $\text{NO}+\text{O}_2$  and the corresponding mapping results of the  $\text{MnO}_x$  (a, a1) and Chlorella@Mn (b, b1) catalysts at  $200^\circ\text{C}$ .



species were generated on the surface of the MnOx catalyst, indicating more severe NO oxidation, and more N<sub>2</sub>O was generated by the reaction of excess NO<sub>2</sub> with NH<sub>3</sub>, which may be one of the reasons for the poor N<sub>2</sub> selectivity of the MnOx catalyst.

The adsorption of NH<sub>3</sub> on the surfaces of the MnOx and Chlorella@Mn were analyzed by in-situ DRIFTS, respectively. As shown in Fig. 13(a, a1), multiple adsorption peaks appeared on the surface of MnOx catalyst with the extension of time, NH<sub>3</sub> adsorption peaks on Lewis acid sites appeared at 1182 cm<sup>-1</sup>, 1248 cm<sup>-1</sup>, and 1612 cm<sup>-1</sup> [66], 1459 cm<sup>-1</sup> was attributed to the bending vibration peak of NH<sub>4</sub><sup>+</sup> on

Brønsted acid site, and 1369 cm<sup>-1</sup> was attributed to the oxide species of adsorbed NH<sub>3</sub>, while the N-H vibrational peak of NH<sub>4</sub><sup>+</sup> appeared at 3032 cm<sup>-1</sup> and the N-H vibrational peak of ligated NH<sub>3</sub> at Lewis acid sites appeared at 3145 cm<sup>-1</sup> and 3331 cm<sup>-1</sup> [67]. As can be seen from Fig. 13(b, b1), more adsorption peaks with higher peak intensities appeared on the surface of Chlorella@Mn, and in addition to the relevant peaks mentioned above, NH<sub>4</sub><sup>+</sup> species peaks on Brønsted acid sites appeared at 1407 cm<sup>-1</sup>, 1742 cm<sup>-1</sup>, 2189 cm<sup>-1</sup>, 2324 cm<sup>-1</sup>, respectively [68], and N-H vibration peak on Lewis acid site at 3262 cm<sup>-1</sup>. After the area integration of the corresponding peaks and the addition

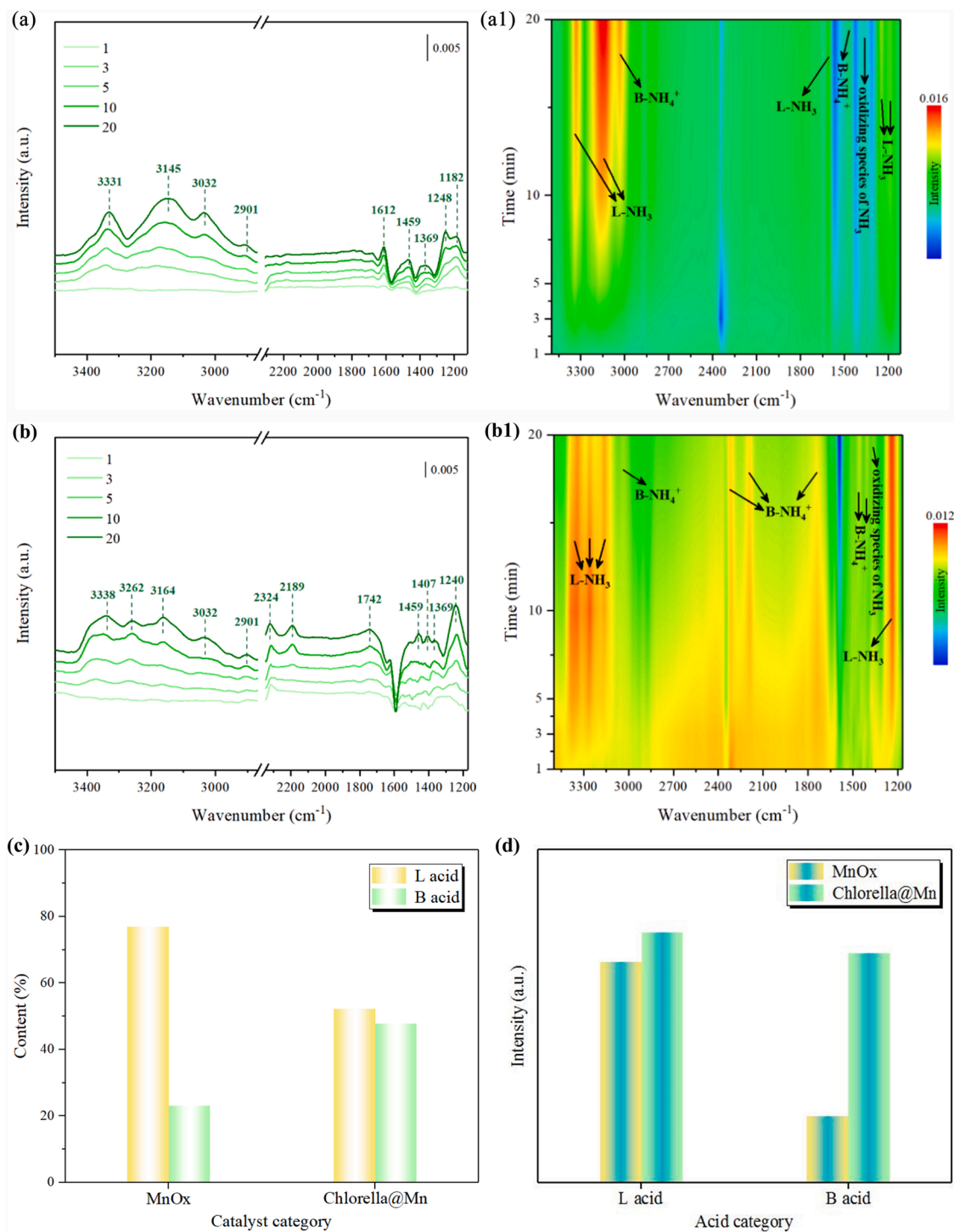


**Fig. 13.** In-situ DRIFT spectra for the adsorption of NH<sub>3</sub> and the corresponding mapping results of the MnOx (a, a1) and Chlorella@Mn (b, b1) catalysts at 200 °C, and the content of acid (c) and the acid amount (d) comparison in both catalysts.



calculation, from Fig. 13(c), it is found that there are more L acids in MnOx, while the contents of B acids and L acids are similar in Chlorella@Mn, which further indicates that Chlorella@Mn surface contains more B acid sites, and it is also found that Chlorella@Mn has more L acids and B acids in Fig. 13(d), combined with the above XPS results, the enhanced acidity may be attributed to the role of phosphoric acid molecules. The above indicates that the surface of Chlorella@Mn possesses more acid sites, and in our previous study [28], it was also verified that Chlorella@Mn catalyst possessed stronger acidity compared to the

MnOx catalyst by  $\text{NH}_3$ -TPD (Fig. S7), which is favorable to promote the adsorption of  $\text{NH}_3$ , which may be one of the reasons for higher low-temperature  $\text{NH}_3$ -SCR activity of Chlorella@Mn catalyst.

Fig. 14(a, b) give the DRIFTS results of adsorption of  $\text{NO}+\text{O}_2$  on the MnOx catalyst surface for 30 min and  $\text{NH}_3$  was passed, it can be clearly found that the peaks intensities at  $1245\text{ cm}^{-1}$ ,  $1379\text{ cm}^{-1}$ ,  $1541\text{ cm}^{-1}$ , and  $1628\text{ cm}^{-1}$  decreased continuously with the increase of reaction time, and some of the peaks even disappeared, indicating that the relevant nitrate species as well as adsorbed  $\text{NO}_2$  were involved in the

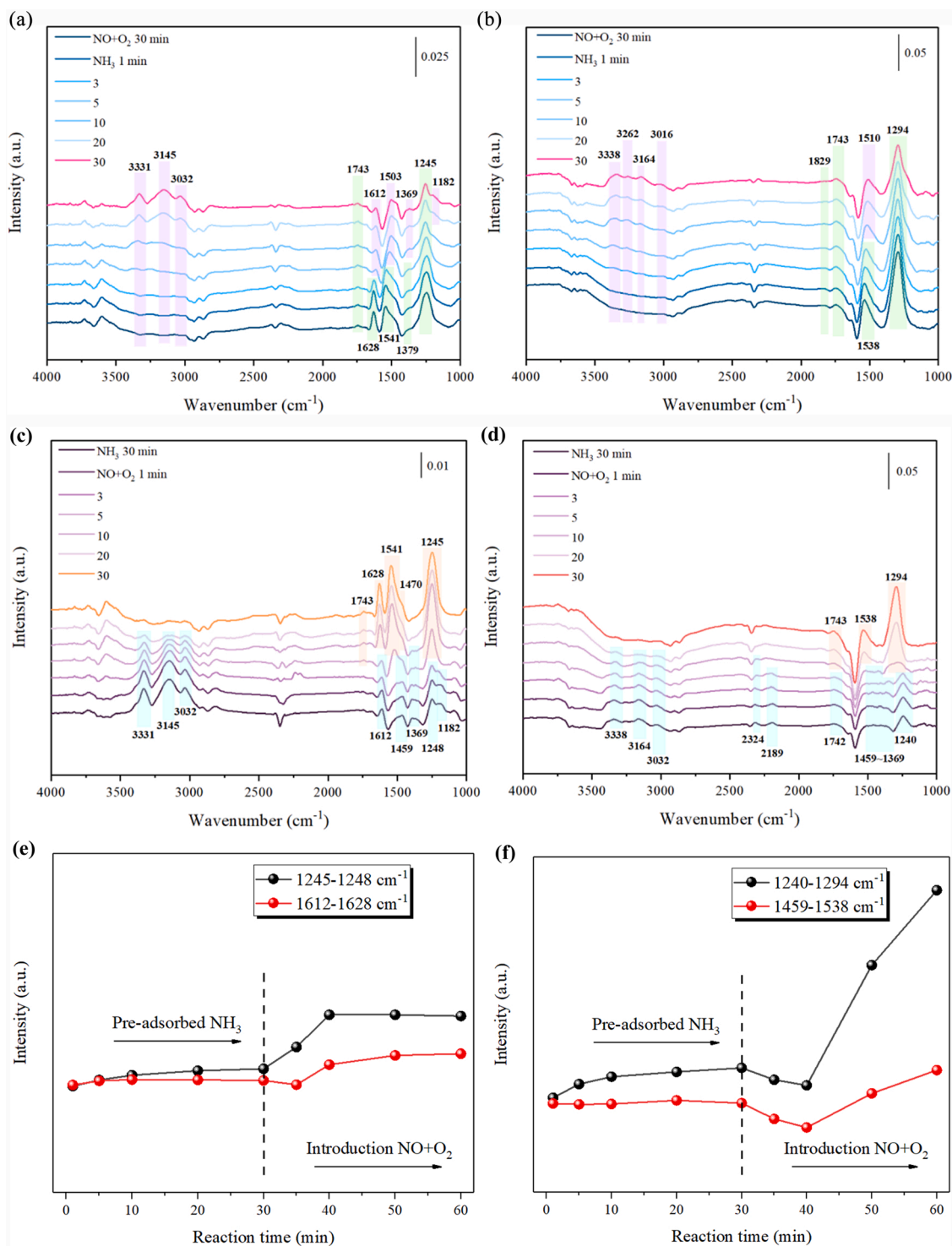


Fig. 14. In-situ DRIFT spectra for the adsorption of  $\text{NH}_3$  after pre-adsorption of  $\text{NO}+\text{O}_2$ : (a) MnOx, (b) Chlorella@Mn, and for adsorption of  $\text{NO}+\text{O}_2$  after pre-adsorption of  $\text{NH}_3$ : (c) MnOx, (d) Chlorella@Mn catalysts and the corresponding adsorption intensity of main peaks: (e) MnOx, (f) Chlorella@Mn catalysts at  $200^\circ\text{C}$ .

reaction that were active species in SCR process, while relevant adsorbed species of  $\text{NH}_3$  appeared at the Lewis and Brønsted acid sites, respectively. The same phenomenon was also observed on the catalyst surface of Chlorella@Mn, where mainly monodentate nitrate ( $1294\text{ cm}^{-1}$ ) and bidentate nitrate ( $1538\text{ cm}^{-1}$ ) were involved in  $\text{NH}_3$ -SCR reaction, both were the main active nitrate species on the surface of Chlorella@Mn. Notably, the presence of  $-\text{NH}_2$  species at  $1503\text{ cm}^{-1}$  and  $1510\text{ cm}^{-1}$  on the surfaces of MnOx and Chlorella@Mn, respectively, which was due to the oxidative dehydrogenation of  $\text{NH}_3$ , while  $-\text{NH}_2$  species were relatively more abundant on the surface of Chlorella@Mn, but  $\text{N}_2$  selectivity was higher relative to that of the MnOx catalyst. Combined with the above, it showed that excessive oxidation of NO was the reason for the poorer  $\text{N}_2$  selectivity of the MnOx catalyst. According to literature research [69], it was speculated that the presence of Ca in Chlorella@Mn inhibited the over-oxidation of NO, allowing the Chlorella@Mn catalyst to possess a relatively higher  $\text{N}_2$  selectivity.

Fig. 14(c, d) shows the adsorption of  $\text{NH}_3$  on the surface of the MnOx and Chlorella@Mn catalysts first for 30 min, respectively, followed by the passage of  $\text{NO}+\text{O}_2$ , and activation species associated with  $\text{NH}_3$  adsorbed at the acid sites of both decreased continuously with time. When  $\text{NO}+\text{O}_2$  was introduced for 30 min, the activation species of  $\text{NH}_3$  almost disappeared, indicating that  $\text{NH}_3$  adsorbed on the surface of both catalysts was involved in SCR reaction, and at the same time, various nitrate species peaks appeared. The number of nitrate species on the surface of Chlorella@Mn was more, mainly monodentate nitrate ( $1294\text{ cm}^{-1}$ ) and bidentate nitrate ( $1538\text{ cm}^{-1}$ ). Similarly, the peaks intensities of  $\text{NH}_3$  and NOx species raise up over time in Fig. 14(e, f), it shows that both MnOx and Chlorella@Mn catalysts have certain adsorption and activation of  $\text{NH}_3$  and NOx, but Chlorella@Mn has stronger adsorption and activation capacity, this may be due to the presence of  $\text{PO}_3$ ,  $\text{PO}_4^{3-}$  and  $\text{P}=\text{O}$ -Mn sites besides Mn-O sites in Chlorella@Mn catalyst, which further enhance the adsorption and activation of  $\text{NH}_3$  and NO, respectively. The above indicates that Chlorella@Mn catalyst has better performance, which is conducive to improving NOx conversion.

In summary, the Chlorella@Mn catalyst has more advantages in NOx conversion compared to the MnOx catalyst. Chlorella@Mn has MnOx,  $\text{P}=\text{O}$ -Mn,  $\text{Ca}_x\text{Mn}_y\text{O}_z$ ,  $\text{PO}_3$  and  $\text{PO}_4^{3-}$  multiple active species, as well as stronger redox performance and acidity, which have stronger adsorption and activation properties for NO and  $\text{NH}_3$  as well as inhibition of NO over-oxidation, which ultimately makes the Chlorella@Mn catalyst have higher NOx conversion,  $\text{N}_2$  selectivity and denitrification stability at low temperature, meanwhile, the Chlorella@Mn catalyst has excellent resistance to  $\text{H}_2\text{O}$  poisoning.

### 3.3. Comparison of Chlorella@Mn and Chlorella catalysts

Since  $\text{NH}_3$ -SCR activity of pure Chlorella catalyst was very low, after testing under the same simulated flue gas conditions, denitrification activity of the catalyst prepared after 24 h of  $\text{Mn}^{2+}$  adsorption was greatly improved by more than 80% at  $100\text{--}225\text{ }^\circ\text{C}$ . It was necessary to further analyze the impact of Mn on Chlorella, so the comparison between Chlorella@Mn and Chlorella was performed by advanced characterization methods to better clarify the physicochemical characteristics of the Chlorella@Mn catalyst prepared by biological method.

#### 3.3.1. Raman and EPR

Raman was a very powerful characterization technology to further obtain detailed information on the lattice vibrational state in the crystal structure and could characterize the diversity of active species on the catalyst surface [70,71]. The structures of Chlorella and Chlorella@Mn were determined by Raman spectra, and the results are shown in Fig. S8. The results showed that the addition of Mn had an effect on original structure of Chlorella, and the catalyst surface of Chlorella@Mn contained more MnOx as well as  $\text{PO}_4^{3-}$ .

As a major structural defect, oxygen vacancy played a more direct role in the generation of surface adsorbed oxygen [72]. EPR can be used to analyze oxygen vacancy content in materials, and to determine the change of oxygen vacancy in Chlorella after binding to Mn, EPR was performed. It can be seen from Fig. S9 that the Chlorella@Mn catalyst possessed more abundant oxygen vacancy. The abundant presence of oxygen vacancy may also further contribute to the breakage of N-O bonds and accelerate the dissociation of NOx [73], which was beneficial to the improvement of deNOx performance in low-temperature  $\text{NH}_3$ -SCR reaction.

#### 3.3.2. TG-DSC

In order to determine the weight loss and heat uptake and release of the catalyst with increasing temperature, TG-DSC were performed on Chlorella and Chlorella@Mn catalysts to further determine the changes of Chlorella before and after binding with Mn. As shown in Fig. S10, the temperature points and weight loss of both were slightly different at  $200\text{--}516\text{ }^\circ\text{C}$ , but both were attributed to the large volatilization of organic components. The intensity of exothermic peak could generally represent crystallization degree of material, the results indicated that the addition of Mn which affected the crystallinity, resulting in a decrease in the degree of crystallization and an increase in disorder. From TG-DSC results, it was concluded that Chlorella produced certain changes after binding with Mn, which was consistent with Raman results.

#### 3.3.3. Acid change

*In-situ* adsorption penetration of  $\text{NH}_3$  was performed on Chlorella and Chlorella@Mn at  $175\text{ }^\circ\text{C}$ , respectively, to determine the change in acidity. As shown in Fig. S11, the results indicated that the Chlorella@Mn catalyst had stronger adsorption performance for  $\text{NH}_3$ , the Chlorella@Mn catalyst was more acidic.

*In-situ* DRIFTS was an effective means to distinguish Lewis and Brønsted acids, which was used to test the  $\text{NH}_3$  adsorption of both catalysts separately for 30 min. The results are shown in Fig. 15(a-b), and it was found that Chlorella@Mn had stronger  $\text{NH}_3$  adsorption peak intensity compared to Chlorella, both had different intensity of Lewis and Brønsted acid sites [74,75], but with stronger L and B acids in Chlorella@Mn due to the addition of Mn [76,77]. Fig. 15(c) and (d) show the corresponding 3D mapping results of *in-situ* DRIFTS of the Chlorella@Mn and Chlorella catalysts respectively, the intensity of each  $\text{NH}_3$  adsorption peak was more vividly and intuitively explained by comparison, further indicating that Chlorella@Mn possessed stronger acidity, which was also consistent with the *in-situ*  $\text{NH}_3$  breakthrough curves results.

After the addition of Mn to the Chlorella catalyst, more MnOx and  $\text{PO}_4^{3-}$  as well as oxygen vacancy appeared on the catalyst surface. Although Chlorella showed basically the same weight loss with the increase of temperature before and after the adsorption of Mn, the original structure of Chlorella changed after the adsorption of Mn, the crystalline degree decreased and the disorder degree increased, meanwhile, Lewis and Brønsted acids enhanced, the above changes indicated that the presence of Mn had a large effect on Chlorella. The combined effect of a large number of active species and oxygen vacancies and stronger acid sites led to a significant promotion of the  $\text{NH}_3$ -SCR reaction, which eventually resulted in an obvious increase in denitrification activity.

## 4. Conclusions

In this study, low-temperature  $\text{NH}_3$ -SCR denitrification catalyst was prepared by biological method, NOx conversion was close to 100% at  $100\text{--}225\text{ }^\circ\text{C}$  with excellent resistance to  $\text{H}_2\text{O}$  poisoning. Chlorella cells could agglomerate and settle after absorbing  $\text{Mn}^{2+}$  for 0.5 h, oxygen-containing groups such as  $\text{C}=\text{O}$ ,  $\text{N}=\text{O}$  and  $\text{P}=\text{O}$  in the cell wall were mainly involved in the adsorption and reaction process of  $\text{Mn}^{2+}$ . The adsorption process mainly included electrostatic interaction,

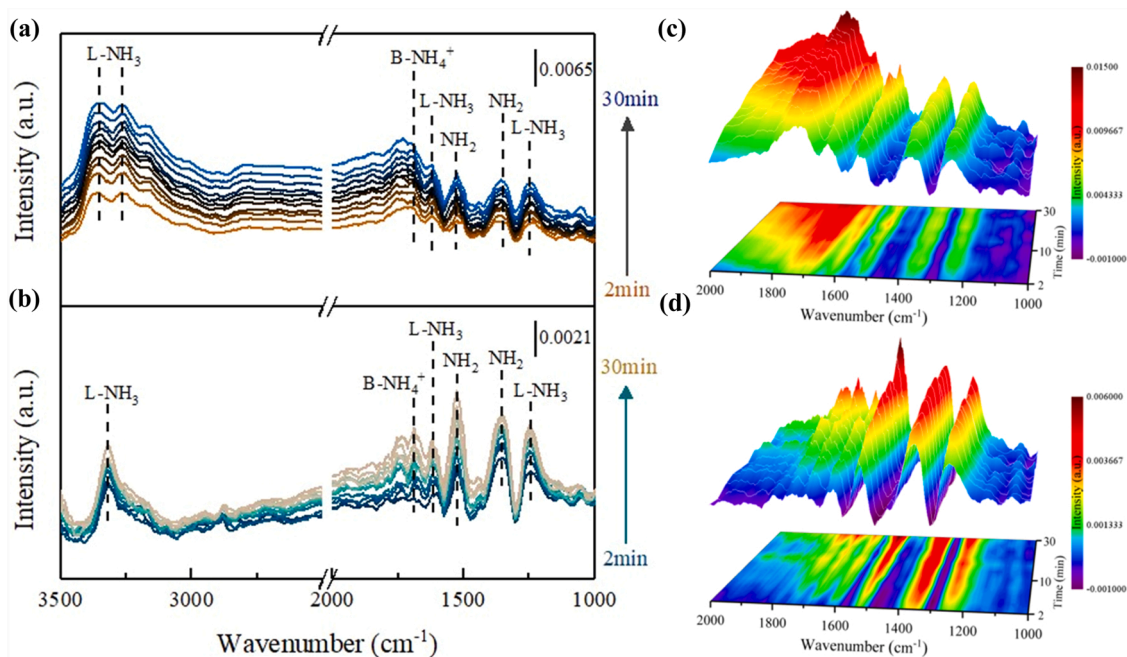


**Fig. 15.** *In-situ* DRIFT spectra for the adsorption of  $\text{NH}_3$  over Chlorella@Mn (a) and Chlorella (b) catalysts at  $175^\circ\text{C}$ , and the corresponding 3D mapping results of Chlorella@Mn (c) and Chlorella (d) catalysts.

complexation/chelation and ion exchange mechanism, in which  $\text{Ca}^{2+}$ ,  $\text{K}^+$  and  $\text{Mg}^{2+}$  were ion exchange objects. Through various characterizations, it was found that at 0.5 h~16 h synthesis time,  $\text{Mn}^{2+}$  and related functional groups were in a slow reaction state, and at 16 h~24 h, violent reaction occurred between the species, and after 24 h, the reaction was completed and reached a relatively stable state. The Chlorella@Mn catalyst prepared at the synthesis time of 24 h had higher  $\text{Mn}^{3+}$  and adsorbed oxygen content on the surface, and possessed stronger adsorption performance for NO and  $\text{NH}_3$ , which was beneficial to improve  $\text{NH}_3$ -SCR activity. Meanwhile, K, Na and Mg on the catalyst surface mainly existed as  $\text{K}_2\text{SO}_4$ ,  $\text{NaPO}_3$  and  $\text{MgSiO}_3$ , respectively, Ca mainly existed in the form of amorphous  $\text{Ca}_x\text{Mn}_y\text{O}_z$ , and Ca could effectively inhibit the over-oxidation of NO, which improved the low-temperature  $\text{N}_2$  selectivity relative to the MnOx catalyst, the above combined forms made the Chlorella@Mn catalyst avoid alkali/alkaline earth metal poisoning.

The Chlorella@Mn catalyst had more active species and oxygen vacancy, stronger Lewis and Brønsted acid sites than the Chlorella catalyst, which facilitated the adsorption and activation of  $\text{NH}_3$ , many of these advantages contributed to the higher denitrification activity of Chlorella@Mn catalyst. Bio-derived  $\text{NH}_3$ -SCR low-temperature catalysts have broad application prospects and research value, and this study will provide some reference for the development of such novel catalysts.

#### CRediT authorship contribution statement

All authors contributed to the study conception, literature, and writing. Prof. Xiaolong Tang, Honghong Yi, Fengyu Gao and Yuansong Zhou put forward the review ideas and organized the writing framework and finally approved the whole content. The first draft was written by Hengheng Liu and refined by Fengyu Gao, and the format was checked by Songjin Ko, Ning Luo. All authors commented on previous versions of the manuscript. The final manuscript was read and approved by all authors for publication.

#### Declaration of Competing Interest

The authors declare that they have no known competing financial

interests or personal relationships that could have appeared to influence the work reported in this paper.

#### Data Availability

The authors do not have permission to share data.

#### Acknowledgments

This work was financially supported by National Natural Science Foundation of China (U20A20130) and Fundamental Research Funds for the Central Universities (FRF-TP-20-03B).

#### Appendix A. Supporting information

Supplementary data associated with this article can be found in the online version at [doi:10.1016/j.apcatb.2023.122651](https://doi.org/10.1016/j.apcatb.2023.122651).

#### References

- [1] M.U. Saeed, N. Hussain, A. Sumrin, A. Shahbaz, S. Noor, M. Bilal, L. Aleya, H.M. N. Iqbal, Microbial bioremediation strategies with wastewater treatment potentialities - A review, *Sci. Total Environ.* 818 (2022), 151754.
- [2] S. Yadav, A. Yadav, N. Bagotia, A.K. Sharma, S. Kumar, Adsorptive potential of modified plant-based adsorbents for sequestration of dyes and heavy metals from wastewater - A review, *J. Water Process Eng.* 42 (2021), 102148.
- [3] T. Kiran Marella, A. Saxena, A. Tiwari, Diatom mediated heavy metal remediation: A review, *Bioresour. Technol.* 305 (2020), 123068.
- [4] X. Chen, M. Zheng, G. Zhang, F. Li, H. Chen, Y. Leng, The nature of dissolved organic matter determines the biosorption capacity of Cu by algae, *Chemosphere* 252 (2020), 126465.
- [5] M. Narayanan, G. Kandasamy, Z. He, S. Kandasamy, A.H. Alfharhan, A. Pugazhendhi, Phytoextraction competence of *J. curcas* L. on ore waste dump of the bauxite mine under the influence of multi potential *Bacillus cereus*, *Environ. Technol. Innov.* 21 (2021), 101221.
- [6] M. Zubair, I. Ihsanullah, H. Abdul Aziz, M. Azmier Ahmad, M.A. Al-Harthi, Sustainable wastewater treatment by biochar/layered double hydroxide composites: Progress, challenges, and outlook, *Bioresour. Technol.* 319 (2021), 124128.
- [7] Y. Zhang, J. Luo, H. Zhang, T. Li, H. Xu, Y. Sun, X. Gu, X. Hu, B. Gao, Synthesis and adsorption performance of three-dimensional gels assembled by carbon nanomaterials for heavy metal removal from water: A review, *Sci. Total Environ.* 852 (2022), 158201.



- [8] A. Rehman, M. Park, S.-J. Park, Current progress on the surface chemical modification of carbonaceous materials, *Coatings* 9 (2019) 103.
- [9] J.Y. Lai, L.H. Ngu, The production cost analysis of oil palm waste activated carbon: a pilot-scale evaluation, *Greenh. Gas. Sci. Technol.* 10 (2020) 999–1026.
- [10] W.S. Chai, J.Y. Cheun, P.S. Kumar, M. Mubashir, Z. Majeed, F. Banat, S.-H. Ho, P. L. Show, A review on conventional and novel materials towards heavy metal adsorption in wastewater treatment application, *J. Clean. Prod.* 296 (2021), 126589.
- [11] Q. Wu, H. Li, X. Hu, Y. Shi, D. Kong, Y. Zhang, B. Mai, D. Zhao, J. Fu, Full-scale evaluation of reversed A<sup>2</sup>/O process for removal of multiple pollutants in sewage, *Chin. Chem. Lett.* 31 (2020) 2825–2830.
- [12] S. Rangabhashiyam, P. Balasubramanian, Characteristics, performances, equilibrium and kinetic modeling aspects of heavy metal removal using algae, *Bioresour. Technol. Rep.* 5 (2019) 261–279.
- [13] S. Kandasamy, M. Narayanan, Z. He, G. Liu, M. Ramakrishnan, P. Thangavel, A. Pugazhendhi, R. Raja, I.S. Carvalho, Current strategies and prospects in algae for remediation and biofuels: An overview, *Biocatal. Agric. Biotechnol.* 35 (2021), 102045.
- [14] P. Bhatt, G. Bhandari, R.F. Turco, Z. Aminikhoei, K. Bhatt, H. Simsek, Algae in wastewater treatment, mechanism, and application of biomass for production of value-added product, *Environ. Pollut.* 309 (2022), 119688.
- [15] J. Hockaday, A. Harvey, S. Velasquez-Orta, A comparative analysis of the adsorption kinetics of Cu<sup>2+</sup> and Cd<sup>2+</sup> by the microalgae *Chlorella vulgaris* and *Scenedesmus obliquus*, *Algal Res.* 64 (2022), 102710.
- [16] L.-g. Wei, R.-t. Guo, J. Zhou, B. Qin, X. Chen, Z.-x. Bi, W.-g. Pan, Chemical deactivation and resistance of Mn-based SCR catalysts for NO<sub>x</sub> removal from stationary sources, *Fuel* 316 (2022), 123438.
- [17] C. Niu, B. Wang, Y. Xing, W. Su, C. He, L. Xiao, Y. Xu, S. Zhao, Y. Cheng, J.-W. Shi, Thulium modified MnO<sub>x</sub>/TiO<sub>2</sub> catalyst for the low-temperature selective catalytic reduction of NO with ammonia, *J. Clean. Prod.* 290 (2021), 125858.
- [18] B. Tian, S. Ma, J. Guo, Y. Zhao, T. Gao, X. Jiang, Superior indicative and regulative function of Fe doping amount for MnO<sub>2</sub> catalyst with an oxygen vacancy in NH<sub>3</sub>-SCR reaction: A DFT + U study, *Appl. Surf. Sci.* 601 (2022), 154162.
- [19] S. Hao, L. Yuling, J. Yang, Construction of Cu-BTC by carboxylic acid organic ligand and its application in low temperature SCR denitration, *Sci. Total Environ.* 820 (2022), 152984.
- [20] Z. Zhang, R. Li, M. Wang, Y. Li, Y. Tong, P. Yang, Y. Zhu, Two steps synthesis of CeTiO<sub>x</sub> oxides nanotube catalyst: Enhanced activity, resistance of SO<sub>2</sub> and H<sub>2</sub>O for low temperature NH<sub>3</sub>-SCR of NO<sub>x</sub>, *Appl. Catal. B Environ.* 282 (2021), 119542.
- [21] K. Kang, X. Yao, Y. Huang, J. Cao, J. Rong, W. Zhao, W. Luo, Y. Chen, Insights into the co-doping effect of Fe<sup>3+</sup> and Zr<sup>4+</sup> on the anti-K performance of CeTiO<sub>x</sub> catalyst for NH<sub>3</sub>-SCR reaction, *J. Hazard. Mater.* 416 (2021), 125821.
- [22] M. Wang, B. Su, S. Ren, W. Liu, J. Yang, Z. Chen, L. Chen, Different lead species deactivation on Mn-Ce activated carbon supported catalyst for low-temperature SCR of NO with NH<sub>3</sub>: Comparison of PbCl<sub>2</sub>, Pb(NO<sub>3</sub>)<sub>2</sub> and PbSO<sub>4</sub>, *J. Colloid Interface Sci.* 622 (2022) 549–561.
- [23] L. Jiang, Y. Liang, W. Liu, H. Wu, T. Aldahri, D.S. Carrero, Q. Liu, Synergistic effect and mechanism of FeO<sub>x</sub> and CeO<sub>x</sub> co-doping on the superior catalytic performance and SO<sub>2</sub> tolerance of Mn-Fe-Ce/ACN catalyst in low-temperature NH<sub>3</sub>-SCR of NO<sub>x</sub>, *J. Environ. Chem. Eng.* 9 (2021), 106360.
- [24] L. Chen, S. Ren, L. Liu, B. Su, J. Yang, Z. Chen, M. Wang, Q. Liu, Catalytic performance over Mn-Ce catalysts for NH<sub>3</sub>-SCR of NO at low temperature: Different zeolite supports, *J. Environ. Chem. Eng.* 10 (2022), 107167.
- [25] L. Chen, S. Ren, X. Xing, J. Yang, J. Li, J. Yang, Q. Liu, Effect of MnO<sub>2</sub> crystal types on CeO<sub>2</sub>/MnO<sub>2</sub> oxides catalysts for low-temperature NH<sub>3</sub>-SCR, *J. Environ. Chem. Eng.* 10 (2022), 108239.
- [26] H. Li, C. Yang, S. Zhang, A. Zhang, Z. Sun, X. Zhang, L. Jin, Z. Song, Indium modified MnO<sub>x</sub> for high-efficient NH<sub>3</sub>-SCR De-NO<sub>x</sub>: Promotional role of indium and its catalytic performance, *J. Environ. Chem. Eng.* 10 (2022), 107462.
- [27] Q. Zhao, B. Chen, J. Li, X. Wang, M. Crocker, C. Shi, Insights into the structure-activity relationships of highly efficient CoMn oxides for the low temperature NH<sub>3</sub>-SCR of NO<sub>x</sub>, *Appl. Catal. B Environ.* 277 (2020), 119215.
- [28] H. Liu, F. Gao, S. Ko, N. Luo, X. Tang, E. Duan, H. Yi, Y. Zhou, Low-temperature NH<sub>3</sub>-SCR performance of a novel *Chlorella*/Mn composite denitrification catalyst, *J. Environ. Sci.* (2022), <https://doi.org/10.1016/j.jes.2022.12.010>.
- [29] R. Soto-Ramirez, M.G. Lobos, O. Cordova, P. Poirrier, R. Chamy, Effect of growth conditions on cell wall composition and cadmium adsorption in *Chlorella vulgaris*: A new approach to biosorption research, *J. Hazard. Mater.* 411 (2021), 125059.
- [30] S.Y. Cheng, P.L. Show, B.F. Lau, J.S. Chang, T.C. Ling, New prospects for modified algae in heavy metal adsorption, *Trends Biotechnol.* 37 (2019) 1255–1268.
- [31] C.E. Flores-Chaparro, L.F. Chazaro Ruiz, M.C. Alfaro de la Torre, M.A. Huerta-Diaz, J.R. Rangel-Mendez, Biosorption removal of benzene and toluene by three dried macroalgae at different ionic strength and temperatures: Algae biochemical composition and kinetics, *J. Environ. Manag.* 193 (2017) 126–135.
- [32] Y. Zhang, Z. Xiong, L. Yang, Z. Ren, P. Shao, H. Shi, X. Xiao, S.G. Pavlostathis, L. Fang, X. Luo, Successful isolation of a tolerant co-flocculating microalgae towards highly efficient nitrogen removal in harsh rare earth element tailings (REEs) wastewater, *Water Res.* 166 (2019), 115076.
- [33] Y. Geng, D. Cui, L. Yang, Z. Xiong, S.G. Pavlostathis, P. Shao, Y. Zhang, X. Luo, S. Luo, Resourceful treatment of harsh high-nitrogen rare earth element tailings (REEs) wastewater by carbonate activated *Chlorococcum* sp. microalgae, *J. Hazard. Mater.* 423 (2022), 127000.
- [34] H. Li, J. Watson, Y. Zhang, H. Lu, Z. Liu, Environment-enhancing process for algal wastewater treatment, heavy metal control and hydrothermal biofuel production: A critical review, *Bioresour. Technol.* 298 (2020), 122421.
- [35] A.K. Priya, A.A. Jalil, S. Vadivel, K. Dutta, S. Rajendran, M. Fujii, M. Soto-Moscoso, Heavy metal remediation from wastewater using microalgae: Recent advances and future trends, *Chemosphere* 305 (2022), 135375.
- [36] C. Song, Z. Liu, C. Wang, S. Li, Y. Kitamura, Different interaction performance between microplastics and microalgae: The bio-elimination potential of *Chlorella* sp. L38 and *Phaeodactylum tricornutum* MASCC-0025, *Sci. Total Environ.* 723 (2020), 138146.
- [37] S. Gu, C.Q. Lan, Biosorption of heavy metal ions by green alga *Neochloris oleoabundans*: Effects of metal ion properties and cell wall structure, *J. Hazard. Mater.* 418 (2021), 126336.
- [38] M.H. Sayadi, O. Rashki, E. Shahri, Application of modified *Spirulina platensis* and *Chlorella vulgaris* powder on the adsorption of heavy metals from aqueous solutions, *J. Environ. Chem. Eng.* 7 (2019), 103169.
- [39] X. Ma, X. Yan, J. Yao, S. Zheng, Q. Wei, Feasibility and comparative analysis of cadmium biosorption by living *Scenedesmus obliquus* FACHB-12 biofilms, *Chemosphere* 275 (2021), 130125.
- [40] Z. Wang, L. Xia, S. Song, M.E. Farías, Y. Li, C. Tang, Cadmium removal from diluted wastewater by using high-phosphorus-culture modified microalgae, *Chem. Phys. Lett.* 771 (2021), 138561.
- [41] F. Yu, W. Nie, W. Zhou, M. Yuan, J. Yan, Y. Hua, Q. Bao, W. Niu, Performance evaluation of Mn-Ce/cordierite catalyst modified by green surfactant to remove NO<sub>x</sub> in underground mines at low temperatures, *J. Environ. Chem. Eng.* 9 (2021), 106499.
- [42] N. Abdel-Raouf, E.N. Sholkamy, N. Bukhari, N.M. Al-Enazi, K.I. Alsamhary, S.H. A. Al-Khat, I.B.M. Ibraheem, Bioremoval capacity of Co<sup>2+</sup> using *Phormidium tenue* and *Chlorella vulgaris* as biosorbents, *Environ. Res.* 204 (2022), 111630.
- [43] V.R. Moreira, Y.A.R. Lebron, S.J. Freire, L.V.S. Santos, F. Palladino, R.S. Jacob, Biosorption of copper ions from aqueous solution using *Chlorella pyrenoidosa*: Optimization, equilibrium and kinetics studies, *Microchem. J.* 145 (2019) 119–129.
- [44] Z. Chen, S. Qiu, Z. Yu, M. Li, S. Ge, Enhanced secretions of algal cell-adhesion molecules and metal ion-binding exoproteins promote self-flocculation of *Chlorella* sp. cultivated in municipal wastewater, *Environ. Sci. Technol.* 55 (2021) 11916–11924.
- [45] M.A. Alam, C. Wan, S.L. Guo, X.Q. Zhao, Z.Y. Huang, Y.L. Yang, J.S. Chang, F. W. Bai, Characterization of the flocculating agent from the spontaneous flocculation microalga *Chlorella vulgaris* JSC-7, *J. Biosci. Bioeng.* 118 (2014) 29–33.
- [46] C. Saka, Metal-free catalysts with phosphorus and oxygen doped on carbon-based on *Chlorella vulgaris* microalgae for hydrogen generation via sodium borohydride methanolysis reaction, *Int. J. Hydrog. Energy* 46 (2021) 5150–5157.
- [47] N. Zhang, L. Li, Y. Guo, J. He, R. Wu, L. Song, G. Zhang, J. Zhao, D. Wang, H. He, A MnO<sub>2</sub>-based catalyst with H<sub>2</sub>O resistance for NH<sub>3</sub>-SCR: Study of catalytic activity and reactants-H<sub>2</sub>O competitive adsorption, *Appl. Catal. B Environ.* 270 (2020), 118860.
- [48] X. Wu, L. Liu, J. Liu, B. Hou, Y. Du, X. Xie, NiMn mixed oxides with enhanced low-temperature deNO<sub>x</sub> performance: Insight into the coordinated decoration of MnO<sub>x</sub> by NiO phase via glycine combustion method, *Appl. Catal. A Gen.* 610 (2021), 117918.
- [49] S. Chen, M.A. Vasiliades, Q. Yan, G. Yang, X. Du, C. Zhang, Y. Li, T. Zhu, Q. Wang, A.M. Efsthathiou, Remarkable N<sub>2</sub>-selectivity enhancement of practical NH<sub>3</sub>-SCR over Co<sub>0.5</sub>Mn<sub>1</sub>Fe<sub>0.25</sub>Al<sub>0.75</sub>O<sub>x</sub>-LDO: The role of Co investigated by transient kinetic and DFT mechanistic studies, *Appl. Catal. B Environ.* 277 (2020), 119186.
- [50] X. Shi, J. Guo, T. Shen, A. Fan, S. Yuan, J. Li, Enhancement of Ce doped La-Mn oxides for the selective catalytic reduction of NO<sub>x</sub> with NH<sub>3</sub> and SO<sub>2</sub> and/or H<sub>2</sub>O resistance, *Chem. Eng. J.* 421 (2021), 129995.
- [51] Y. Li, X. Leng, S. Ma, T. Zhang, F. Yuan, X. Niu, Y. Zhu, Effects of Mo addition on the NH<sub>3</sub>-SCR of NO reaction over Mo<sub>0.5</sub>Mn<sub>1</sub>Ti<sub>0.5</sub>O<sub>x</sub> (a=0.2, 0.4, 0.6 and 0.8): Synergistic action between redox and acidity, *Catal. Today* 339 (2020) 254–264.
- [52] J. Cao, S. Rohani, W. Liu, H. Liu, Z. Lu, H. Wu, L. Jiang, M. Kong, Q. Liu, X. Yao, Influence of phosphorus on the NH<sub>3</sub>-SCR performance of CeO<sub>2</sub>-TiO<sub>2</sub> catalyst for NO<sub>x</sub> removal from co-incineration flue gas of domestic waste and municipal sludge, *J. Colloid Interface Sci.* 610 (2022) 463–473.
- [53] Y. Zeng, Z. Wu, L. Guo, Y. Wang, S. Zhang, Q. Zhong, Insight into the effect of carrier on N<sub>2</sub>O formation over MnO<sub>2</sub>/MO<sub>x</sub> (M = Al, Si and Ti) catalysts for selective catalytic reduction (SCR) of NO<sub>x</sub> with NH<sub>3</sub>, *Mol. Catal.* 488 (2020), 110916.
- [54] S. Cheng, J. Shao, B. Huang, J. Guan, L. Zhou, Promotion effect of urchin-like MnO<sub>x</sub>/PrO<sub>x</sub> hollow core-shell structure catalysts for the low-temperature selective catalytic reduction of NO with NH<sub>3</sub>, *RSC Adv.* 10 (2020) 13855–13865.
- [55] A. Guo, K. Xie, H. Lei, V. Rizzotto, L. Chen, M. Fu, P. Chen, Y. Peng, D. Ye, U. Simon, Inhibition effect of phosphorus poisoning on the dynamics and redox of Cu active sites in a Cu-SSZ-13 NH<sub>3</sub>-SCR catalyst for NO<sub>x</sub> reduction, *Environ. Sci. Technol.* 55 (2021) 12619–12629.
- [56] S. Thirakkal, X. Zhang, Covalent functionalization of two-dimensional black phosphorus nanosheets with porphyrins and their photophysical characterization, *Mater. Chem. Front.* 5 (2021) 2824–2831.
- [57] H. Kang, J. Wang, J. Zheng, W. Chu, C. Tang, J. Ji, R. Ren, M. Wu, F. Jing, Solvent-free elaboration of Ni-doped MnO<sub>x</sub> catalysts with high performance for NH<sub>3</sub>-SCR in low and medium temperature zones, *Mol. Catal.* 501 (2021), 111376.
- [58] J.-R. Youn, M.-J. Kim, S.-J. Lee, I.-S. Ryu, H.C. Yoon, S.K. Jeong, K. Lee, S.G. Jeon, The influence of CNTs addition on Mn-Ce/TiO<sub>2</sub> catalyst for low-temperature NH<sub>3</sub>-SCR of NO, *Catal. Commun.* 152 (2021), 106282.
- [59] G. Li, B. Wang, H. Wang, J. Ma, W.Q. Xu, Y. Li, Y. Han, Q. Sun, Fe and/or Mn oxides supported on fly ash-derived SBA-15 for low-temperature NH<sub>3</sub>-SCR, *Catal. Commun.* 108 (2018) 82–87.



- [60] L. Chen, S. Ren, W. Liu, J. Yang, Z. Chen, M. Wang, Q. Liu, Low-temperature  $\text{NH}_3$ -SCR activity of M (M = Zr, Ni and Co) doped  $\text{MnO}_x$  supported biochar catalysts, *J. Environ. Chem. Eng.* 9 (2021), 106504.
- [61] L. Liu, S. Su, D. Chen, T. Shu, X. Zheng, J. Yu, Y. Feng, Y. Wang, S. Hu, J. Xiang, Highly efficient  $\text{NH}_3$ -SCR of  $\text{NO}_x$  over  $\text{MnFeW/Ti}$  catalyst at low temperature:  $\text{SO}_2$  tolerance and reaction mechanism, *Fuel* 307 (2022), 121805.
- [62] J. Chen, P. Fu, D. Lv, Y. Chen, M. Fan, J. Wu, A. Meshram, B. Mu, X. Li, Q. Xia, Unusual positive effect of  $\text{SO}_2$  on Mn-Ce mixed-oxide catalyst for the SCR reaction of  $\text{NO}_x$  with  $\text{NH}_3$ , *Chem. Eng. J.* 407 (2021), 127071.
- [63] C. Peng, R. Yan, H. Peng, Y. Mi, J. Liang, W. Liu, X. Wang, G. Song, P. Wu, F. Liu, One-pot synthesis of layered mesoporous ZSM-5 plus Cu ion-exchange: Enhanced  $\text{NH}_3$ -SCR performance on Cu-ZSM-5 with hierarchical pore structures, *J. Hazard. Mater.* 385 (2020), 121593.
- [64] Y. Liu, F. Gao, S. Ko, C. Wang, H. Liu, X. Tang, H. Yi, Y. Zhou, Superior catalytic performance within  $\text{H}_2\text{O}$ -vapor of W-modified  $\text{CoMn}_2\text{O}_4/\text{TiO}_2$  catalyst for selective catalytic reduction of  $\text{NO}_x$  with  $\text{NH}_3$ , *Chem. Eng. J.* 434 (2022), 134770.
- [65] C. Wang, F. Gao, S. Ko, H. Liu, H. Yi, X. Tang, Structural control for inhibiting  $\text{SO}_2$  adsorption in porous MnCe nanowire aerogel catalysts for low-temperature  $\text{NH}_3$ -SCR, *Chem. Eng. J.* 434 (2022), 134729.
- [66] S. Yu, X. Niu, Z. Song, X. Huang, Y. Peng, J. Li, Improvement of  $\text{Al}_2\text{O}_3$  on the multi-pollutant control performance of  $\text{NO}_x$  and chlorobenzene in vanadia-based catalysts, *Chemosphere* 289 (2022), 133156.
- [67] Y. Bai, J. Zhu, H. Luo, Z. Wang, Z. Gong, R. Zhao, W. Wu, K. Zhang, Study on  $\text{NH}_3$ -SCR performance and mechanism of Fe/Mn modified rare earth concentrate, *Mol. Catal.* 514 (2021), 111665.
- [68] Y. Li, S. Cai, P. Wang, T. Yan, J. Zhang, D. Zhang, Improved  $\text{NO}_x$  reduction over phosphate-modified  $\text{Fe}_2\text{O}_3/\text{TiO}_2$  catalysts via tailoring reaction paths by in situ creating alkali-poisoning sites, *Environ. Sci. Technol.* 55 (2021) 9276–9284.
- [69] Y. Liu, T. Gu, X. Weng, Y. Wang, Z. Wu, H. Wang, DRIFT studies on the selectivity promotion mechanism of Ca-modified Ce-Mn/TiO<sub>2</sub> catalysts for low-temperature NO reduction with  $\text{NH}_3$ , *J. Phys. Chem. C* 116 (2012) 16582–16592.
- [70] T. Zhang, Y. Zhang, P. Ning, H. Wang, Y. Ma, S. Xu, M. Liu, Q. Zhang, F. Xia, The property tuning of  $\text{NH}_3$ -SCR over iron-tungsten catalyst: Role of calcination temperature on surface defect and acidity, *Appl. Surf. Sci.* 538 (2021), 147999.
- [71] S. Guo, H. Wang, W. Yang, H. Fida, L. You, K. Zhou, Scalable synthesis of Ca-doped  $\alpha\text{-Fe}_2\text{O}_3$  with abundant oxygen vacancies for enhanced degradation of organic pollutants through peroxymonosulfate activation, *Appl. Catal. B Environ.* 262 (2020), 118250.
- [72] J. Liu, X. Li, R. Li, Q. Zhao, J. Ke, H. Xiao, L. Wang, S. Liu, M. Tadé, S. Wang, Facile synthesis of tube-shaped Mn-Ni-Ti solid solution and preferable Langmuir-Hinshelwood mechanism for selective catalytic reduction of  $\text{NO}_x$  by  $\text{NH}_3$ , *Appl. Catal. A Gen.* 549 (2018) 289–301.
- [73] X. Yao, L. Chen, J. Cao, Y. Chen, M. Tian, F. Yang, J. Sun, C. Tang, L. Dong, Enhancing the de $\text{NO}_x$  performance of  $\text{MnO}_x/\text{CeO}_2\text{-ZrO}_2$  nanorod catalyst for low-temperature  $\text{NH}_3$ -SCR by  $\text{TiO}_2$  modification, *Chem. Eng. J.* 369 (2019) 46–56.
- [74] H. Xie, D. Shu, T. Chen, H. Liu, X. Zou, C. Wang, Z. Han, D. Chen, An in-situ DRIFTS study of Mn doped  $\text{FeVO}_4$  catalyst by one-pot synthesis for low-temperature  $\text{NH}_3$ -SCR, *Fuel* 309 (2022), 122108.
- [75] Z. Fu, G. Zhang, W. Han, Z. Tang, The water resistance enhanced strategy of Mn based SCR catalyst by construction of  $\text{TiO}_2$  shell and superhydrophobic coating, *Chem. Eng. J.* 426 (2021), 131334.
- [76] G. Yang, H. Zhao, X. Luo, K. Shi, H. Zhao, W. Wang, Q. Chen, H. Fan, T. Wu, Promotion effect and mechanism of the addition of Mo on the enhanced low temperature SCR of  $\text{NO}_x$  by  $\text{NH}_3$  over  $\text{MnO}_x/\gamma\text{-Al}_2\text{O}_3$  catalysts, *Appl. Catal. B Environ.* 245 (2019) 743–752.
- [77] Y. Shi, H. Yi, F. Gao, S. Zhao, Z. Xie, X. Tang, Facile synthesis of hollow nanotube  $\text{MnCoO}_x$  catalyst with superior resistance to  $\text{SO}_2$  and alkali metal poisons for  $\text{NH}_3$ -SCR removal of  $\text{NO}_x$ , *Sep. Purif. Technol.* 265 (2021), 118517.